



Blood endothelial ALK1-BMP4 signaling axis regulates adult hair follicle stem cell activation

Kefei Nina Li, Gopal Chovatiya , Daniel Youngjoo Ko, Sripad Sureshbabu & Tudorita Tumber* 

Abstract

Blood vessels can play dual roles in tissue growth by transporting gases and nutrients and by regulating tissue stem cell activity via signaling. Correlative evidence implicates skin endothelial cells (ECs) as signaling niches of hair follicle stem cells (HFSCs), but functional demonstration from gene depletion of signaling molecules in ECs is missing to date. Here, we show that depletion of the vasculature-factor *Alk1* increases BMP4 secretion from ECs, which delays HFSC activation. Furthermore, while previous evidence suggests a lymphatic vessel role in adult HFSC activation possibly through tissue drainage, a blood vessel role has not yet been addressed. Genetic perturbation of the ALK1-BMP4 axis in all ECs or the lymphatic ECs specifically unveils inhibition of HFSC activation by blood vessels. Our work suggests a broader relevance of blood vessels, adding adult HFSCs to the EC functional repertoire as signaling niches for the adult stem cells.

Keywords Alk1; BMP4; endothelial cells; hair follicle stem cells; vascular niche
Subject Categories Cardiovascular System; Skin; Stem Cells & Regenerative Medicine

DOI 10.15252/emboj.2022112196 | Received 25 July 2022 | Revised 28 February 2023 | Accepted 2 March 2023 | Published online 30 March 2023

The EMBO Journal (2023) 42: e112196

Introduction

The molecular cross-talking between adult stem cells (SCs) and their niches is important for proper tissue homeostasis, SC activation, and SC maintenance. Endothelial cells (ECs) composing the vasculature have been reported as signaling niches in several adult SC systems, including blood, bone, and neural (Ramasamy *et al*, 2015; Comazzetto *et al*, 2021). Highly regenerative tissues such as the skin might be especially dependent upon a dual coordinated role of blood vessels in both cargo transport (e.g. gases, nutrients, waste products, and cells) and in signaling to the resident epithelial SCs to regulate their activity. While hair follicle stem cells (HFSCs) signal outward to organize the neighboring microenvironment including vasculature, (Li & Tumber, 2021) aside from some correlative evidence from us (Li *et al*, 2019) and others (Yoon & Detmar, 2022), no EC signal to date has been directly demonstrated to act on HFSCs by

direct genetic targeting in ECs. Moreover, while recent evidence demonstrates that killing ECs from the skin lymphatic vasculature affects hair follicle stem cell (HFSC) activation from quiescence during the hair homeostatic cycle, possibly due to perturbed tissue drainage (Skobe & Detmar, 2000; Gur-Cohen *et al*, 2019; Peña-Jimenez *et al*, 2019; Li & Tumber, 2021), the role of blood vessels in HFSC activation has not yet been unequivocally identified.

The hair follicle (HF) undergoes synchronous phases of remodeling known as telogen (rest), anagen (growth), and catagen (destruction). Quiescent HFSCs located in the hair bulge and primed HFSCs located in the hair germ at telogen become activated from quiescence and produce the hair bulb and hair shaft at anagen; then HFSCs return to quiescence, and the HF bulbs regress back during catagen (Fuchs *et al*, 2004; Tumber, 2012; Li & Tumber, 2021; Fig EV1). The hair bulge is located permanently in the skin dermis, while the hair germ found at the junction with hypodermis grows in size at anagen turning into the hair bulb and driving more than triple hypodermis expansion that fills up with engorging fat cells and with blood vessels tightly wrapped around the new hair bulbs (Chase *et al*, 1953; Durward & Rudall, 1958; Mecklenburg *et al*, 2000; Cotsarelis, 2006; Zwick *et al*, 2018; Houschyar *et al*, 2020; Li & Tumber, 2021; Fig EV1). During catagen, as the HF bulbs and the hypodermis regresses, the skin vasculature is reoriented forming a horizontal plexus underneath the hair germ (HPuHG; Li *et al*, 2019; Fig EV1). This vascular plexus disperses and remodels at anagen, moving vertically and around the growing HFs into the hypodermis (Li *et al*, 2019; Li & Tumber, 2021; Fig EV1). Previously, we genetically depleted the *Activin receptor like type 1 (Alk1)* in ECs of both blood and lymphatic vessels in *Cdh5-CreERT2* driven *Alk1* knockout mice and described three correlative effects: an unusually dense HPuHG, a delay in HFSCs activation, and a simultaneous increase in skin BMP4 protein levels (Li *et al*, 2019; Fig 1A). While BMP signaling plays a prominent role in HFSC activation via the BMPRIa receptor expression in the skin epithelium (Plikus *et al*, 2008; Yi, 2017), a BMP role in skin vasculature cross talk with hair follicles has not been directly explored until now.

Here we use the Alk1-BMP axis as a testing paradigm in mice and demonstrate for the first time by direct genetic depletion in ECs that inductive signals secreted from blood vessel ECs can inhibit HFSC activation, impacting their gene expression and delaying the hair homeostatic cycle. This uncovers the blood vessels' EC capability as *bona fide* endocrine niches promoting quiescence of HFSCs,

thus expanding their known repertoire as signaling niches for adult stem cell activity.

Results

Alk1 loss perturbs all skin endothelial cell populations and affects cell migration genes

Previously we showed that pan-EC *Alk1* KO mice (Cdh5-CreERT2xAlk1^{fllox/fllox} from here on Alk1^{EndoKO}) showed perturbed CD31+ skin vasculature morphology, with a dense HPuHG, and a delay in HFSC activation and hair cycle progression into anagen (Li et al, 2019; Fig 1A). To understand which EC compartments are affected by *Alk1* loss and to examine the mechanisms by which *Alk1* works in ECs, we first performed single-cell RNA-seq (scRNA-seq) of sorted skin ECs. For this, we crossed the Rosa26R-lox-STOP-lox-tdTomato reporter mice with the Alk1^{EndoKO} mice and induced Cre recombination with Tamoxifen (TM) at postnatal day (PD)17 to label the ECs (Fig 1A and B). We then FACS-purified tdTomato-positive ECs from PD25 Alk1^{EndoKO} mice dorsal skin (Fig EV2A) and performed single-cell RNA-seq (scRNA-seq) using the 10x Genomics platform. Wild type (WT) and CT (Cre negative/TM-injected) mice at PD25 are at anagen with an activated hair germ (HG) and sometimes lower bulge that proliferates; in contrast, in the PD25 Alk1^{EndoKO} skin HFs are at telogen with no proliferation in HFs (Li et al, 2019), while the vasculature may have a mixed telogen/anagen phenotype. Therefore, to account for possible hair cycle stage effects on EC transcriptomes, we used Harmony integration methods (Korsunsky et al, 2019) of scRNA-seq data to compare the Alk1^{EndoKO} ECs with CT samples from Cdh5-CreERT2;tdTomato+ mice injected with TM at PD17 and sacrificed at both telogen (PD20) and anagen (PD32; preprint: Chovatiya et al, 2023). All Alk1^{EndoKO} and CT samples were of high quality, with 13 major clusters detected in both CT and Alk1^{EndoKO} using Uniform Manifold Approximation and Projection (UMAP) analysis (Fig EV2B–E). A small (~ 1%) EC proliferative cluster was found in CT but not detected in the Alk1^{EndoKO} samples, likely due to low cell resolution limits. Based on known marker expression, we identified and eliminated the contaminating non-EC clusters and reclustered five EC populations through the Seurat pipeline (Hao et al, 2021). These clusters were: artery, vein, two BV capillary populations, lymphatic capillary, and lymphatic collecting vessel (Figs 1C and EV2F and G). The total EC number for telogen CT, anagen CT, and Alk1^{EndoKO} sample is 2,543, 7,498, and 3,103, respectively. The expression of *Alk1* mRNAs was detectable in all CT EC populations at telogen and anagen, suggesting that *Alk1* may play a role both in skin BVs and LVs during the hair cycle (Fig EV2H). A detailed comparative analysis of telogen vs. anagen samples will be published elsewhere (preprint: Chovatiya et al, 2023), while here we focus on *Alk1* role in BV and LV ECs.

To understand the effect of *Alk1* loss in BV and LV EC populations, we examined differentially expressed genes (DEGs) cluster by cluster in Alk1^{EndoKO} relative to both telogen and anagen CT samples. While EC clusters showed relatively modest DEG in CT anagen vs. CT telogen samples, all Alk1^{EndoKO} ECs had unique and substantial changes in transcriptomic profiles relative to both stages (Fig 1D and E). Categorization of these DEG into biological processes using the Panther database (Mi et al, 2019, 2021) revealed genes related to metabolism (16%), signaling (7%), cellular localization (6.7%),

locomotion (1.7%), and cell adhesion (1.2%), among others (Fig EV3A). Interestingly, ribosomal markers such as Rpl9 and Rps2 have much higher expression in Alk1^{EndoKO} compared with both CT groups, suggesting potentially elevated biosynthesis (Fig EV3B). Gene Ontology (GO) analysis of DEGs revealed many pathways changed in the Alk1^{EndoKO} samples, which included metabolism, extracellular matrix organization, and cell adhesion, suggesting that *Alk1* loss globally perturbs EC homeostasis (Fig EV3C). Finally, heatmap of the relative expression of the combined list of 1,722 DEGs showed the Alk1^{EndoKO} ECs clusters together, standing out from the two CT groups at both telogen and anagen (Fig 1E; Source Data). The BVs and particularly the BV capillaries were the most changed among all the EC populations (Fig 1D and E; Source Data). DEG heat map shows complex patterns of association, with some genes changed in a similar fashion in all Alk1 EC clusters relative to at least one CT group, and other genes changing specifically in distinct EC population (Fig 1E; Source Data). These results constitute a rich database for future mining of the *Alk1*-induced mechanisms in different skin EC populations.

To examine the common effects in BVs and LVs, we intersected the DEG list across all EC population, which revealed that 20 core genes significantly changed in all the Alk1^{EndoKO} clusters relative to both telogen and anagen control groups (Fig 1F). Among the up-regulated genes, *Ahnak* (Haase et al, 2017) has implication in vascular healing; *Txnip* (Meszaros et al, 2021) contributes to unorganized and tortuous vessels in tumors; and *Ppfbp1* (Norrmen et al, 2010) maintains the integrity of LVs. Furthermore, *Anxa2* (Luo et al, 2017) was shown to support microvascular integrity in the lung and was downregulated in our Alk1^{EndoKO} skin ECs (Fig 1F). The remaining genes (*Tns1* (Shih et al, 2015), *Map3k6* (Eto et al, 2009), *Timp3* (Qi & Anand-Apte, 2015), *Selenop* (Marciel & Hoffmann, 2017), *Lcn2* (Wu et al, 2015), *Ctsh* (Bühler et al, 2013), *Anxa5* (Sun et al, 2018), and *Vim* (Ostrowska-Podhorodecka et al, 2022)) were associated with angiogenesis and EC migration, in line with previous reports that demonstrated the *Alk1*'s role in these processes (Oh et al, 2000; Larrivé et al, 2012; Rochon et al, 2016). Furthermore, collective enrichment analysis for GO term of ECs migration (GO: 0043542) showed significant ($P < 0.003$) changes in all clusters with significant decreases in Alk1^{EndoKO} BVs, especially in artery and capillaries, and a small but significant increase in the lymphatic capillary (Fig 1G). This result suggests that *Alk1* may affect migration of skin ECs, as they become remodeled during the hair cycle from telogen to anagen (Durward & Rudall, 1958; Mecklenburg et al, 2000; Li & Tumber, 2021).

In conclusion, our single-cell RNA-seq data revealed that *Alk1* loss in pan-ECs induced significant gene expression changes in both the LV and BV populations and their respective subpopulations. The DEG genes show complex patterns of regulation in the different clusters and point to many cellular responses including metabolism, angiogenesis, cell adhesion, and especially EC migration.

Alk1 modulates EC localization/mobilization during hair cycle but not their proliferation

Next, we asked if EC migration, proliferation, or both contributed to Alk1^{EndoKO} vascular phenotype during hair cycle, as suggested by our scRNA-seq data here and by reports of *Alk1* role in EC migrations in other tissues or in injured skin (Oh et al, 2000; Larrivé et al, 2012;

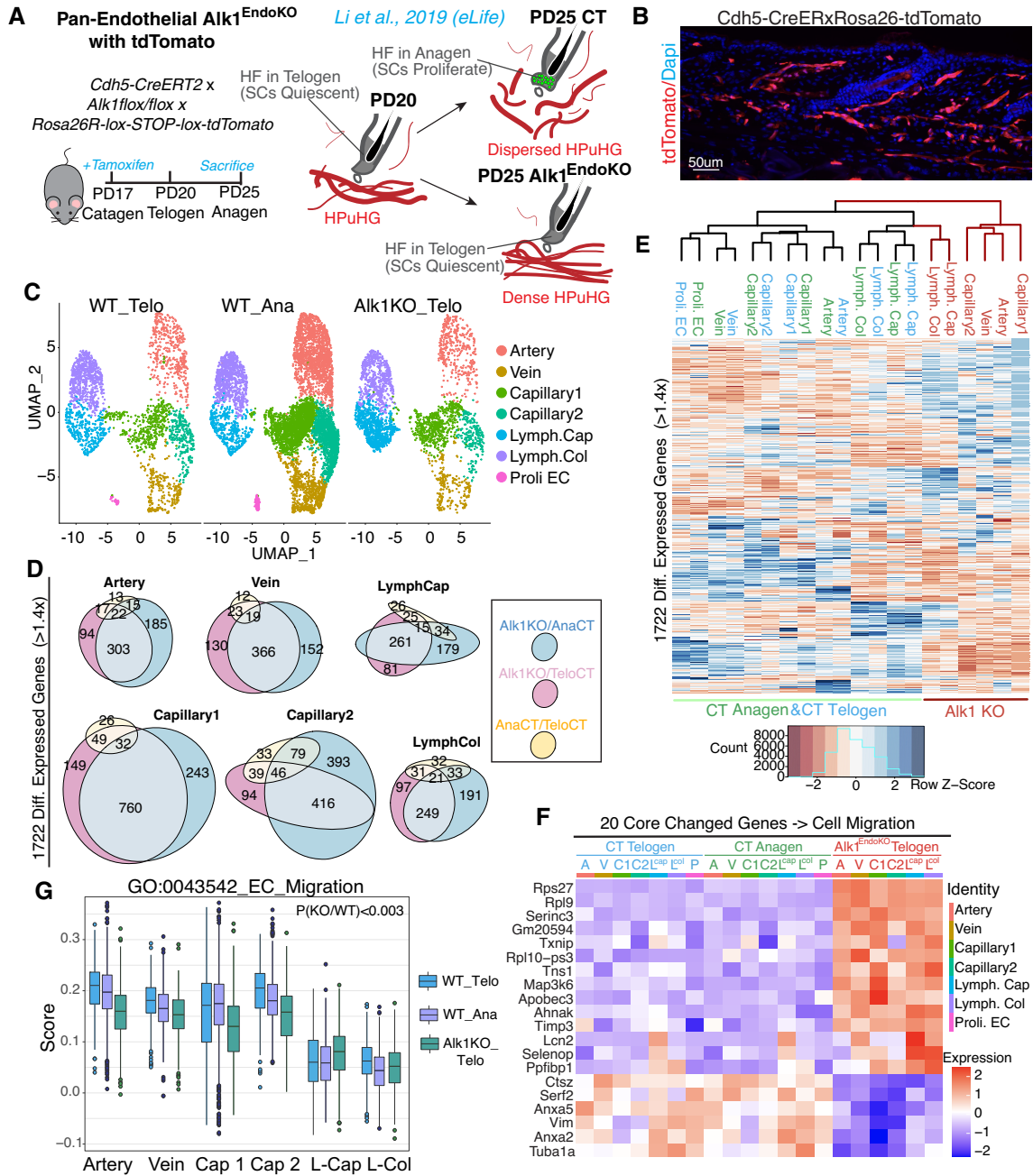


Figure 1. Alk1 loss perturbs gene expression in all skin endothelial cell types and affects migration-related pathway.

A Induction scheme of mice used for FACS (left) and a cartoon summary of previous work (Li et al, 2019) showing PD25 Alk1^{EndoKO} mice have delayed HFSC activation and dense HPuHG (right).

B 12 μm skin section of mouse used for FACS showing tdTomato labeling of the vasculature.

C UMAP of clustered skin endothelial cell types in telogen WT, anagen WT, and Alk1^{EndoKO} mice. N = 2 for each group, and total EC number for telogen CT, anagen CT, and Alk1^{EndoKO} sample is 2,543, 7,498, and 3,103 respectively.

D Venn diagram showing differentially regulated genes in Alk1^{EndoKO} relative to both telogen and anagen CT samples and between the CT samples at the two stages by FindMarker function in Seurat.

E Heat map of 1,722 differentially expressed genes (DEG) shows clustering of Alk1^{EndoKO} endothelial cell population away from both telogen and anagen samples.

F Heatmap showing relative expressions of 20 core genes in all clusters at all stages in CT and Alk1^{EndoKO} mice.

G Migration score in different EC clusters in telogen, anagen CT, and Alk1^{EndoKO} based on expression levels of genes in GO terms GO_Migration (GO: 0043542). Nonparametric comparisons for each pair done cluster by cluster using Wilcoxon Method rendered P values that were less than 0.003 for Alk1^{EndoKO} samples when compared with both WT telogen and anagen samples. The central bands represent medians. The boxes define the first to the third quartiles, and the whiskers show the largest/smallest value that's within 1.5 inter-quartile range within the hinge of the box. N = 2 for each group.

Source data are available online for this figure.

Rochon *et al.*, 2016). We previously reported a significant increase in the $Alk1^{EndoKO}$ CD31+ area in the HPuHG, a defined hypodermis region below the hair germ, which we previously quantified in skin sections (Li *et al.*, 2019). Here we qualitatively illustrate this dense HPuHG phenotype with our first whole mount cleared skin tissue and 3D confocal microscopy and image surface rendering (Fig 2A; raw images shown in Fig EV4A). We found HFs arrested at telogen in the $Alk1^{EndoKO}$ skin by PD25 when CT skin was at early anagen, as expected from our previous analysis (Li *et al.*, 2019; Fig EV4B). Furthermore, inspection of the Z-optical stacks of the whole mount images revealed for the first time the presence of tortuous vasculature structures within the HPuHG area of the $Alk1^{EndoKO}$ (Fig 2B), not previously reported in the absence of skin injury (Park *et al.*, 2009).

To examine the possible changes in ECs numbers and/or proliferation in $Alk1^{EndoKO}$ skin, we performed co-immunofluorescence (IF) staining and confocal microscopy for Cdh5, Erg (a nuclear EC marker; Nikolova-Krstevski *et al.*, 2009), and Ki67. We used 8- μ m skin sections from CT skin at PD20 (telogen), PD25 (early anagen), and in some cases PD32 (anagen) and $Alk1^{EndoKO}$ at PD25 (Figs 2C and EV4C). We found that the number of Cdh5+ cells increased in the HPuHG area of the PD25 $Alk1^{EndoKO}$ skin when compared with both telogen and early anagen CT skin (Fig 2D). The increased number of Cdh5+ cells in the HPuHG of the $Alk1^{EndoKO}$ skin was not accompanied by increased in Ki67+ proliferative ECs in the HPuHG (Fig 2E) nor in the total skin area (Fig 2F) of the $Alk1^{EndoKO}$ mice. Furthermore, prolonged BrdU pulse (PD17–24; Fig EV4D) followed by quantification of the fraction of BrdU+/Cdh5+ cells (Fig 2G) showed statistically insignificant differences in the fraction of proliferative cells. EC numbers increase from telogen to full anagen by ~30% in CT mice, as previously reported (Mecklenburg *et al.*, 2000; Yano *et al.*, 2001; Li *et al.*, 2019), and EC numbers in $Alk1^{EndoKO}$ skin at PD25 were also somewhat increased (Fig EV4F). Importantly, the ratio of EC located in the HPuHG area vs. total skin area decreased at the telogen–early anagen transition, as expected from dispersal of vasculature at this stage (Li *et al.*, 2019), but it nearly doubled in the $Alk1^{EndoKO}$ relative to PD25 early anagen controls (Fig 2H). This result together with the absolute increase in EC number in the $Alk1^{EndoKO}$ HPuHG (Fig 2D) suggests defects in EC mobilization out of the HPuHG areas at the telogen-to-anagen transition, with impaired vascular remodeling of the HPuHG. These defects may

result in accumulation of ECs in the HPuHG, which can explain the increased density of the HPuHG in the $Alk1^{EndoKO}$ skin in the absence of increased proliferation. In fact, *Alk1* is a well-known regulator of EC migration in cultured skin ECs and in other tissue systems (Rochon *et al.*, 2016; Park *et al.*, 2021). Together, these findings indicate that *Alk1* regulates skin vasculature remodeling in hair cycle, at least in part by promoting EC mobilization or migration from the HPuHG area out into the hypodermis and dermis areas at the transition from telogen to anagen (Fig 2I).

***Alk1* loss affects the remodeling of blood vessels and lymphatic capillaries in hair cycle**

Our scRNA-seq data suggest that $Alk1^{EndoKO}$ affects both blood vessels (BVs) and lymphatic vessels (LVs), while the hair cycle-related morphology evaluation demonstrates overall impairment in EC rearrangement/mobilization out of the HPuHG area (Figs 1 and 2). To understand what morphological changes occur specifically in BVs vs. LVs, we first stained 12 μ m skin sections of PD25 $Alk1^{EndoKO}$ and CT skin at both telogen and early anagen for a BV marker, EMCN (Gur-Cohen *et al.*, 2019) that does not overlap with VEGFR3, an LV marker (Fig EV4G). Quantification of percentage of EMCN+/CD31+ area showed that the HPuHG is predominately composed of BVs (Fig 3A–D). Moreover, the EMCN+ BV area was significantly increased in the $Alk1^{EndoKO}$ HPuHG on a level similar to the increase we reported for the CD31+ vasculature (Li *et al.*, 2019; Fig 3E). The LVs, as defined by the EMCN–/CD31+ vasculature, were not changed in the HPuHG area of the $Alk1^{EndoKO}$ skin (Fig 3F). These data demonstrate that it was the BVs' impaired remodeling and mobilization that primarily contributed to the observed dense HPuHG phenotype in the $Alk1^{EndoKO}$ skin.

Next, we examined how LVs were affected by the *Alk1* loss in skin ECs. To capture the entirety of LVs, we performed IF staining and confocal microscopy on 60 μ m thick skin sections for LYVE1 (lymphatic capillary) and VEGFR3 (lymphatics capillaries + collecting vessels) markers (Fig 3G–J). In CT skin, the lymphatic capillaries caliber (total capillary area/side length adjacent to HF) at telogen (PD20) and early anagen (PD25) was small, but increased noticeably by full anagen (PD32), adopting a more fenestrated appearance (Fig 3G–I, quantified in 3K and see Fig EV4H for

Figure 2. *Alk1* modulates vascular spatial rearrangement but not EC proliferation in adult skin.

- A 3D reconstruction of skin whole mount samples of wild-type mice at telogen (PD20) and early anagen (PD25) and $Alk1^{EndoKO}$ and stained for CD31 (surface rendering, red) and KRT14 marking hair follicles (green). White dotted line highlights the HPuHG area.
- B Single optical plane in the HPuHG of wild-type mice and $Alk1^{EndoKO}$ mice showing dramatic vascular defect in $Alk1^{EndoKO}$ mice. Severely tangled and tortuous vasculatures were outlined in white dotted rectangles.
- C 8 μ m skin section of Cre- control (CT) and $Alk1^{EndoKO}$ mice stained for Cdh5 (red), Ki67 (green), Erg (white), and Dapi (blue). Examples of Cdh5/Ki67 double positive cells were enlarged in the white dotted inset for visualization purposes.
- D–G Error bars represent standard deviation. Each bar represents one individual mouse, and each dot represents measurement from one image. $N = 3$ mice per group, and $n = 9–16$ images per mouse. Restricted maximum likelihood (REML) analysis with unbounded variance components was used as statistical test, and individual mouse was treated as random effect to take into the account of mouse-to-mouse variability. (D) Quantification of number of ECs in HPuHG area from (C). (E) Percentage of proliferative ECs (percentage of Ki67+ Cdh5+ cells in total Cdh5+ cells) in HPuHG from (C). (F) Percentage of proliferative ECs (percentage of Ki67+/Cdh5+ cells in total skin Cdh5+ cells) from C and Fig EV4B. (G) Percentage of proliferative ECs (percentage of BrdU+ Cdh5+ cells in total Cdh5+ cells) in total skin from PD17–24 BrdU-pulsed CT and $Alk1^{EndoKO}$ mice; images shown in Fig EV4C and D.
- H Percentage of ECs in the HPuHG in total skin ECs. Error bar represents standard deviation. Each dot represents measurement from one image. $N = 3$ mice per group, $n = 36/31/48/27$ images total for each group respectively. Unpaired student's *t*-test was used to calculate *P*-values.
- I Schematic showing control mice, when hair follicle transitions from telogen to anagen; ECs proliferate and are mobilized out of the HPuHG, causing its dispersal. In $Alk1^{EndoKO}$ mice, ECs have decreased mobilization and similar level of proliferation as CT mice. This leads to a dense HPuHG with increased number of ECs. HPuHG region was outlined by blue dotted lines, vasculature was shown in red, and Ki67 positive HFSCs were shown in green.

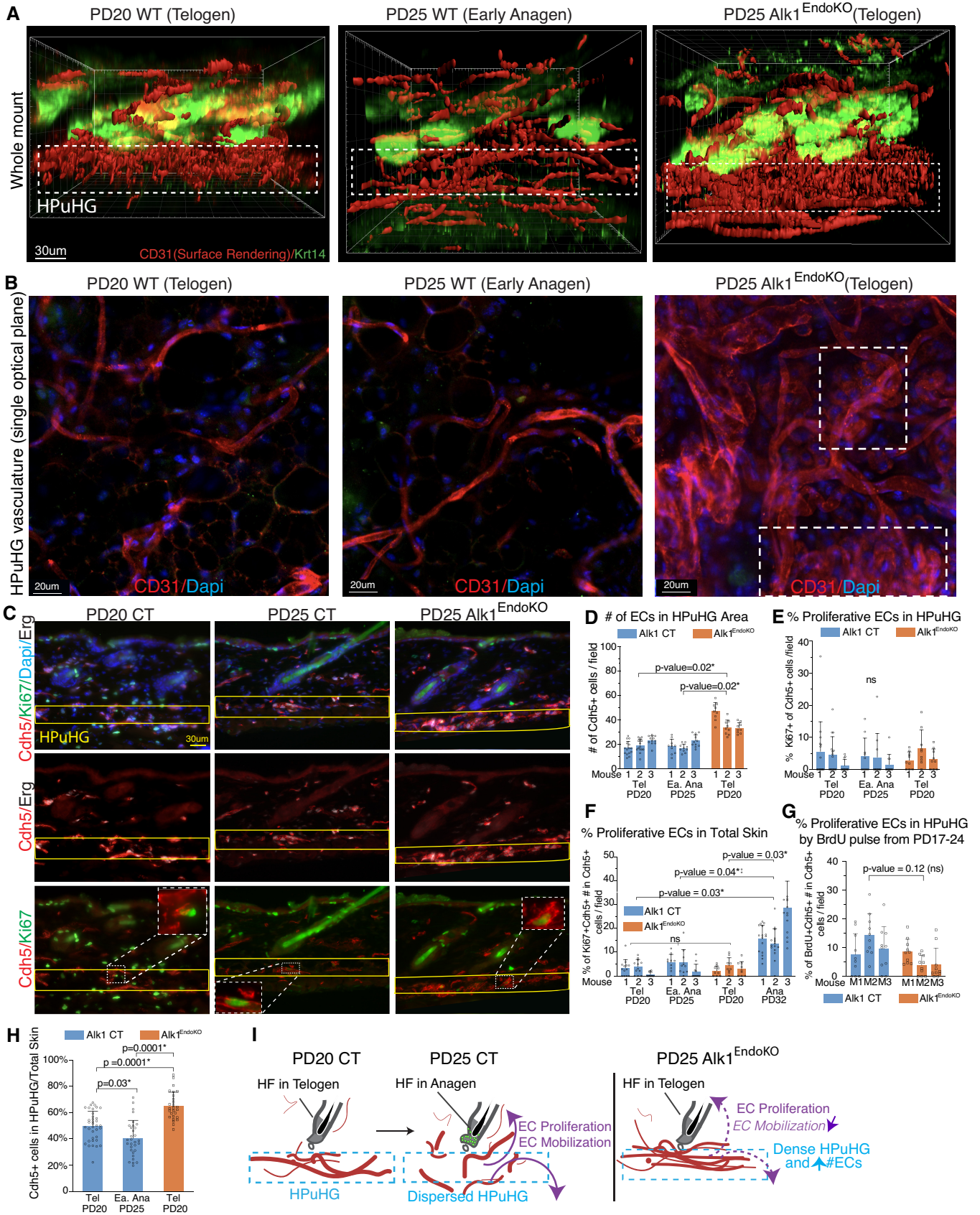


Figure 2.

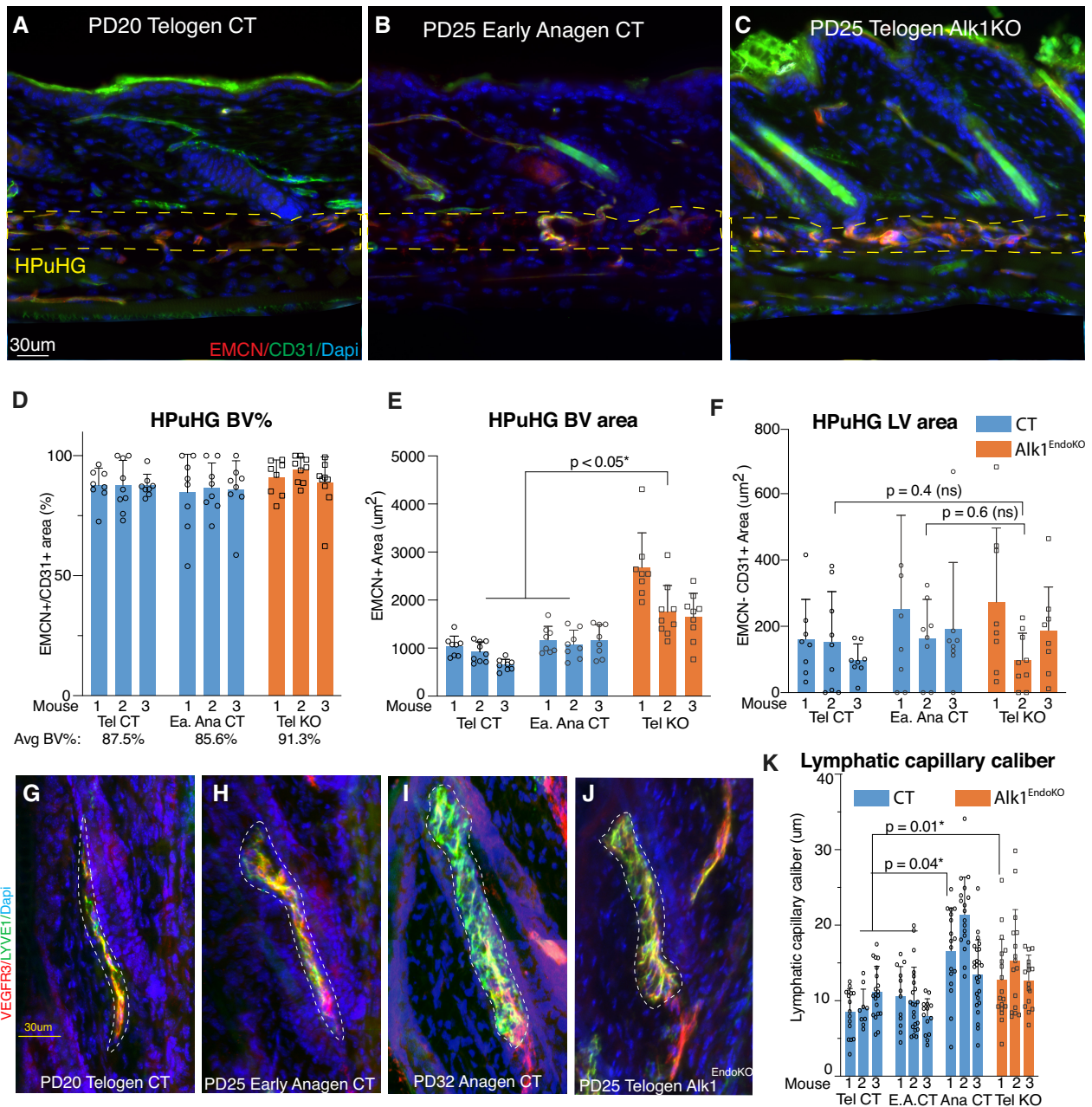


Figure 3. Alk1 loss in endothelial cells induced morphological changes in both blood and lymphatic skin vasculature.

A–C Immunofluorescence staining images of 12 µm skin section from PD17 induced PD20 telogen CT, PD25 early anagen CT, and PD25 telogen Alk1^{EndoKO} mice stained for Endomucin (EMCN, red), CD31 (green), and Dapi (blue). HPUHG region was outlined in yellow dotted lines.

D–F Error bars represent standard deviation. Each bar represents one individual mouse, and each dot represents measurement from one image. *N* = 3 mice per group, and *n* = 8–9 images per mouse. Restricted maximum likelihood (REML) analysis with unbounded variance components was used to calculate *P*-values and individual mouse was treated as random effect to take into the account of mouse-to-mouse variability. (D) Quantification of EMCN+/CD31+ area from images like those in (A–C), shown as percentage of BV in the HPUHG. (E) Quantification of absolute EMCN+ area (e.g. BV area) in HPUHG in images like those in (A–C). (F) Quantification of EMCN-/CD31+ area from images like those in (A–C) as LV area in the HPUHG.

G–J Maximum projection through optical Z-stacks of 60 µm skin sections from mice TM-induced at PD17 and sacrificed at PD20 telogen CT, PD25 early anagen CT, PD32 Anagen CT, and PD25 telogen Alk1^{EndoKO} mice stained for VEGFR3 (red), LYVE1 (green), and Dapi (blue). Lymphatic capillaries were outlined in white dotted lines.

K Quantification of lymphatic capillary caliber from images like those in G–J in PD20 telogen CT, PD25 early anagen CT, and PD25 telogen Alk1^{EndoKO} mice (see Fig EV4H for methods). Error bars represent standard deviation. Each bar represents one individual mouse, and each dot represents measurement from one lymphatic capillary. *N* = 3 mice per group, and *n* = 9–25 measurements per mouse. Restricted maximum likelihood (REML) analysis with unbounded variance components was used to calculate *P*-values, and individual mouse was treated as random effect to take into the account of mouse-to-mouse variability.

method), in line with previous reports (Gur-Cohen *et al*, 2019; Peña-Jimenez *et al*, 2019). Interestingly, although the hair follicles in the $Alk1^{EndoKO}$ skin were still in telogen by PD25, the lymphatic capillaries had already adopted a full anagen morphology, not seen in CT mice until later in the hair cycle, by PD32 (Fig 3G-K). This suggests that $Alk1$ loss in ECs accelerates the opening of the lymphatic capillaries, which advance prematurely into an anagen-like morphology by PD25. Since in $Alk1^{EndoKO}$ PD25 skin, the hair follicles themselves are arrested at telogen while the lymphatic capillaries progressed to anagen, these data demonstrate a decoupling of the hair cycle-related lymphatic capillary remodeling from the remodeling of the hair follicle itself.

To summarize, $Alk1$ loss in BV and LV ECs affects the morphology and remodeling of both BVs and LVs during the hair cycle. Specifically, BVs, which we show are the predominant HPuHG component, appeared denser in the HPuHG area of the $Alk1^{EndoKO}$ skin accounting for the known skin vasculature phenotype in these mice. When taken together with our scRNA-seq that shows migration-related gene changes and with our EC counts (Figs 1 and 2), these data suggest that in the absence of $Alk1$, BV ECs are not mobilized properly out of the HPuHG area during the telogen-to-anagen transition. Furthermore, the lymphatic capillary morphology was also changed in the $Alk1^{EndoKO}$ mice resulting in a premature anagen-like morphology, with fenestrated appearance and widening of the caliber, while the HFs remained behind in telogen. This data indicates that $Alk1$ loss caused a decoupling between the remodeling of the hair follicle and the lymphatic capillary remodeling related to hair cycle. This result prompted us to investigate in more detail the potential contribution of $Alk1$ loss in the LVs to HFSC activation.

$Alk1$'s role in lymphatic vessels affects their morphology but does not control HFSC activation

Lymphatic capillaries are remodeled during HFSC activation, but how this remodeling affects hair cycle is still unclear, as LV cell ablation both inhibited and promoted HFSC activation in two competing studies (Gur-Cohen *et al*, 2019; Peña-Jimenez *et al*, 2019; Li & Tumber, 2021). To understand whether the abnormal anagen-like morphology of lymphatic capillaries in $Alk1^{EndoKO}$ mice may affect HFSC activation, we knocked out $Alk1$ using the *Prox1-CreERT2* lymphatic specific driver. This *Prox1-CreERT2* driver (Srinivasan *et al*, 2007) had reportedly high induction efficiency in the skin (Gur-Cohen *et al*, 2019), and this was also confirmed in our tamoxifen-injected *Prox1-CreERT2* × *Rosa26R-lox-STOP-lox-tdTomato* mice and VEGFR3 staining (Fig 4A-C). The *Prox1-CreERT2* × $Alk1^{flox/flox}$ mice were then induced with TM at PD17 to produce a lymphatic specific $Alk1$ knockout line ($Alk1^{LymphKO}$; Fig 4D). LYVE1 and VEGFR3 IF staining of 60 μm skin sections at PD25 and confocal microscopy revealed an accelerated anagen-like lymphatic capillary morphology in the $Alk1^{LymphKO}$ when compared with CT mice, similar to the one induced in the pan-endothelial $Alk1^{EndoKO}$ (Fig 4E and F). This indicated both that the $Alk1$ KO in lymphatic capillaries is efficient and that the morphological changes are directly caused by $Alk1$ loss in lymphatic ECs and not by secondary effects from BVs. The lymphatic collecting vessel area did not differ between $Alk1$ CT and $Alk1^{LymphKO}$, as also seen in the pan-endothelial $Alk1^{EndoKO}$ skin (Figs EV4I and EV5A). Importantly, unlike the

pan-EC $Alk1^{EndoKO}$ (Li *et al*, 2019), in the $Alk1^{LymphKO}$ skin, the hair follicles were not telogen-arrested, and instead most hair follicles had already progressed into Anagen I and II (Fig 4G and H, and Table 1, $n = 6/4$ mice analyzed for CT/KO group). Furthermore, the HPuHG area remained undisturbed in the $Alk1^{LymphKO}$ and CT skin (Fig EV5B and C), as expected since $Alk1$ was not depleted in BVs. In conclusion, the data show that $Alk1$ loss in LVs alone induces strong morphological changes in the lymphatic capillaries, but these changes did not delay HFSC activation. Therefore, it follows that the delay in HFSC activation observed in the pan-EC $Alk1^{EndoKO}$ must originate from $Alk1$ loss in the skin BVs and not in the LVs.

Bulk RNA-seq of HFSCs showed elevated BMP signaling signatures

Having characterized in depth the role of $Alk1$ in various skin vasculature compartments during hair cycle, we next asked how $Alk1$ loss in the ECs perturbs the HFSCs leading to their delayed activation. For this we performed bulk RNA-seq of HFSCs, FACS sorted from skin as previously described (Osorio *et al*, 2008) using PD17-induced CT and $Alk1^{EndoKO}$ mice and sacrificed at PD20, when all mice were still at telogen and all HFSCs are prepared for activation but are still quiescent (Figs 5A and B, and EV5D). At this early telogen stage, a hair germ has already formed from the bulge; the lower bulge will continue to contribute quiescent HFSCs to the hair germ until early anagen, when hair germ/lower bulge and next all bulge cells are sequentially activated (Zhang *et al*, 2009, 2010; Hsu *et al*, 2014).

Raw sequencing data of the sorted HFSCs were processed through the DESeq2 pipeline (Love *et al*, 2014) to generate a HFSC differential expressed gene (DEG) list. We then filtered the gene list according to the following criteria: (i) minimum read count of 50 in at least one sample, (ii) average twofold change between CT and $Alk1^{EndoKO}$ HFSCs, and (iii) consistent DEG changes in each pair of CT versus $Alk1^{EndoKO}$ mice. This generated a stringent list of 161 HFSC DEGs, including 60 upregulated and 101 downregulated genes in $Alk1^{EndoKO}$ compared with CT (Fig 5C; Source Data) on which we performed Gene Set Enrichment Analysis (GSEA) to extract the GO pathways induced in HFSCs by $Alk1$ loss in the ECs. Pathway analysis showed that among the most prominent downregulated pathways and DEG, many were cell cycle related (Fig 5D, top; Source Data). Given the early onset of these gene expression changes in the HFSCs of $Alk1^{EndoKO}$ mice, at PD20, the stage when CT HFSCs are still quiescent, these changes are likely a cause (not a consequence) of the subsequent HFSCs activation delay. Additionally, biosynthesis and several metabolic processes were upregulated in the $Alk1^{EndoKO}$ HFSCs relative to CT (Fig 5D; Source Data). Responses to different metabolic compounds were also changed, as follows: responses to oxygen- and nitrogen-containing compounds were upregulated, while responses to organic cyclic compound and lipids were downregulated (Fig 5D; Source Data). This reflects an overall abnormal transcriptomic state inflicted on the quiescent HFSCs within just 4 days upon $Alk1$ loss from ECs.

Although not tested directly in skin vasculature, BMP signaling is a well-known potent quiescence factor of HFSC in the skin (Botchkarev & Sharov, 2004; Lee & Tumber, 2012). We previously found BMP4 upregulated at the protein level in the $Alk1^{EndoKO}$ skin (Li *et al*, 2019). Therefore, to see if transcriptomic changes in our

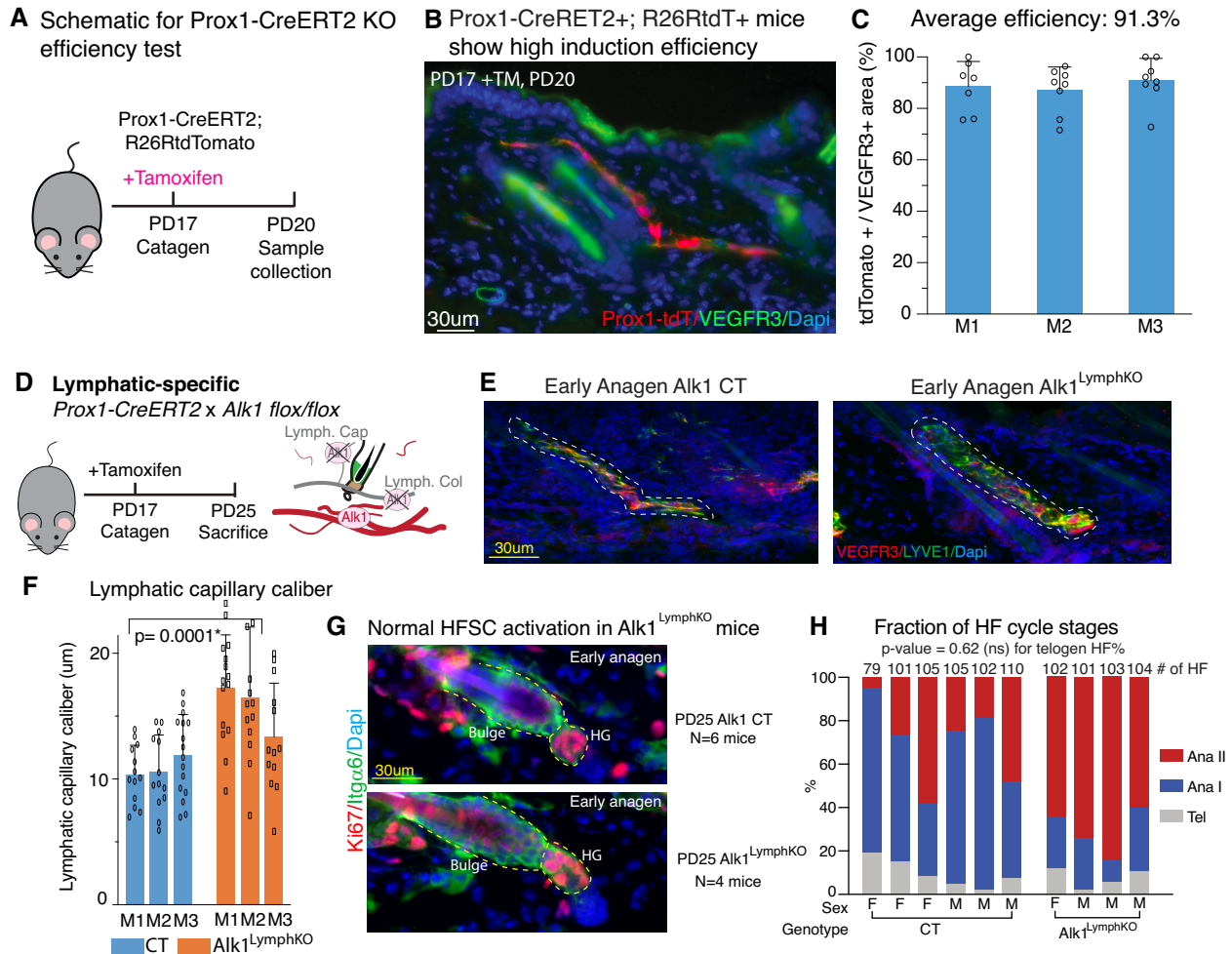


Figure 4. Alk1 loss specifically in lymphatic vessels promotes premature anagen-like lymphatic capillary morphology while hair follicles remain behind in the hair cycle.

A Schematic showing the induction of Prox1-CreERT2; Rosa26R-lox-STOP-lox-tdTomato mice with TM at PD17 and sacrificed at PD20 for efficiency test.

B Immunofluorescence image of 12 μm skin section from mice treated as shown in A, stained for VEGFR3 (green) and Dapi (blue).

C Quantification of tdTomato+ / VEGFR3+ area from images like those in B, shows high induction efficiency. Error bars represent standard deviation. Each bar represents one individual mouse, and each dot represents measurement from one image. $N = 3$ mice, and $n = 7-8$ images per mouse.

D Schematic showing the induction of Alk1^{LymphKO} mice at PD17 and sacrificed at PD25.

E Maximum projection image of 60 μm skin section of PD17 induced PD25 CT and Alk1^{LymphKO} mice stained for VEGFR3 (red), LYVE1 (green) and Dapi (blue). Lymphatic capillaries were outlined in white dotted lines.

F Quantification of lymphatic capillary caliber from images like those in D in CT and Alk1^{LymphKO} mice (see Fig EV4H for methods). Error bars represent standard deviation. Each bar represents one individual mouse, and each dot represents measurement of one lymphatic capillary. $N = 3$ mice per group, and $n = 13-16$ measurements per mouse. Restricted maximum likelihood (REML) analysis with unbounded variance components was used as statistical test, and individual mouse was treated as random effect to take into the account of mouse-to-mouse variability.

G Immunofluorescence images of 12 μm skin section of PD17 induced PD25 CT and Alk1^{LymphKO} mice stained for Ki67 (red), Itga6 (green) and Dapi (blue) showing representative hair follicle. Hair follicles were outlined with yellow dotted lines. Note Ki67+ cells in the hair germ (HG) area indicative of HFSC activation. Telogen hair follicle is defined as no Ki67 in the hair germ. Anagen I is defined as ≤ 7 Ki67+ cells in the unenlarged hair germ. Anagen II is defined as > 7 Ki67+ cells in the hair germ or enlarged hair germ with changed shape that starts to enclose the DP. Experiments were repeated at least 2 times with at least 3 skin sections/each mouse analyzed with $N = 6/4$ mice/group. See Table 1 for quantification detail.

H Quantification of hair follicle percentage of PD17-induced PD25 CT and Alk1^{LymphKO} mice at telogen, anagen I, and anagen II stages. P -value was generated from Student's t -test.

HFSCs may be consistent with elevated BMP signaling, we compared our HFSCs DEGs with lists of HFSC-induced BMP target genes previously identified (Genander *et al*, 2014) either by RNA-seq from the *Bmpr1a* KO mice (black text in Fig 5E) or by pSMAD1/5 CHIP-seq (gray text in Fig 5E). We found that $\sim 30\%$ (49/161) of our DEGs were previously reported HFSC BMP target genes, and they

changed here in a direction largely consistent with increased BMP signaling. Among those 33% (16/49 genes) are BMP target genes that are cell cycle related. In addition, we also identified 9% (14/161) genes that are cell-cycle regulators not previously associated with BMP signaling, and in total there were 19% (30/161) out of all DEGs cell cycle related (Fig 5F). As we further divided our DEGs

Table 1. Quantification of mouse hair cycle stages.

Mouse ID	Sex	Genotype	Age	Region	Image analyzed	Total HF analyzed	Ki67+ HF	Tel	Ana I	Ana II
G410.01	F	Alk1 BMP4 dKO	PD25	Upper	25	84	13	71	10	3
G410.02	F	Alk1 BMP4 dKO	PD25	Upper	26	84	9	75	3	6
G410.06	F	Alk1 BMP4 dKO	PD25	Upper	22	75	18	57	16	2
G961.03	F	Alk1 BMP4 dKO	PD25	Upper	22	72	26	46	10	16
G303.04	M	Alk1 BMP4 dKO	PD25	Upper	21	83	33	50	26	7
G303.09	M	Alk1 BMP4 dKO	PD25	Upper	33	101	33	68	20	13
G79.03	F	Alk1 KO	PD25	Upper	20	80	1	79	1	0
G430.08	F	Alk1 KO	PD25	Upper	19	74	2	72	2	0
G633.03	F	Alk1 KO	PD25	Upper	28	106	1	105	0	1
G430.04	M	Alk1 KO	PD25	Upper	23	101	1	100	1	0
F430.03	M	Alk1 KO	PD25	Upper	17	73	0	73	0	0
G230.02	M	Alk1 KO	PD25	Upper	22	75	0	75	0	0
G79.02	F	CT	PD25	Upper	29	79	64	15	60	4
G430.07	F	CT	PD25	Upper	25	101	86	15	59	27
G410.04	F	CT	PD25	Upper	23	105	97	9	35	61
G79.05	M	CT	PD25	Upper	38	105	100	5	74	26
G410.03	M	CT	PD25	Upper	20	102	100	2	81	19
G410.05	M	CT	PD25	Upper	32	110	103	8	49	53
G665.05	F	BMP4 KO	PD25	Upper	28	101	92	9	33	59
G570.07	F	BMP4 KO	PD25	Upper	20	96	72	24	27	46
G665.02	M	BMP4 KO	PD25	Upper	25	104	82	22	12	70
G648.05	F	BMP2;4 dKO	PD25	Upper	24	100	92	8	9	83
H306.01	F	BMP2;4 dKO	PD25	Upper	28	100	99	1	14	85
H306.04	F	BMP2;4 dKO	PD25	Upper	28	98	92	6	22	70
F923.03	M	BMP2;4 dKO	PD25	Upper	25	102	91	11	46	45
F923.04	M	BMP2;4 dKO	PD25	Upper	28	105	99	6	36	63
G648.03	M	BMP2;4 dKO	PD25	Upper	29	77	59	18	12	47
F1020.02	F	Prox1 Alk1 KO	PD25	Upper	19	102	85	12	24	66
F1020.01	M	Prox1 Alk1 KO	PD25	Upper	18	101	99	2	24	75
F1020.03	M	Prox1 Alk1 KO	PD25	Upper	22	103	94	6	10	87
F1020.07	M	Prox1 Alk1 KO	PD25	Upper	23	104	93	11	30	63

into gene function categories, both the BMP signaling target genes and cell cycle genes constituted a significant large fraction when compared with any other category changed in HFSC by loss of Alk1

in ECs (Fig 5E and F). These findings pointed us to examine in more depth BMP signaling as a potential pathway regulated by *Alk1* in ECs that may affect HFSC activation in hair cycle.

Figure 5. Alk1 loss in the skin endothelial cells altered HFSC pathways including metabolism, cell cycle genes, and BMP signaling.

- A Schematic showing the workflow to generate HFSC differentially expressed genes (DEGs). PD17 induced CT and Alk1^{EndoKO} mice were sacrificed and their sorted HFSCs were processed for bulk RNA-seq.
- B Immunofluorescence image of 12 μ m skin section from CT and Alk1^{EndoKO} mice used for RNA-seq stained for Ki67 (red) and Dapi (blue) shows that HFSCs are in quiescence.
- C Raw RNA-seq data processing and filtering, rendered 161 DEGs with a cutoff of fold change > 2, which were used for subsequent analysis. Heatmap showing the expression of the 161 DEGs across all samples, in which 60 genes were upregulated (UP) in Alk1^{EndoKO} and 101 genes were downregulated (DN).
- D Selected GSEA pathways showing cell cycle and metabolism gene changes in HFSCs.
- E Table of BMP downstream genes and cell cycle related genes. In BMP signaling genes, BMP downstream genes identified by RNA-seq from the BMPRIa KO mice were written in black, and those identified by pSMAD1/5 CHIP-seq are written in gray. Underscored genes were identified by both RNA-seq and CHIP-seq (Genander et al, 2014).
- F Gene function categories of the 161 DEGs, and percentage of BMP signaling and cell cycle related genes.

Source data are available online for this figure.

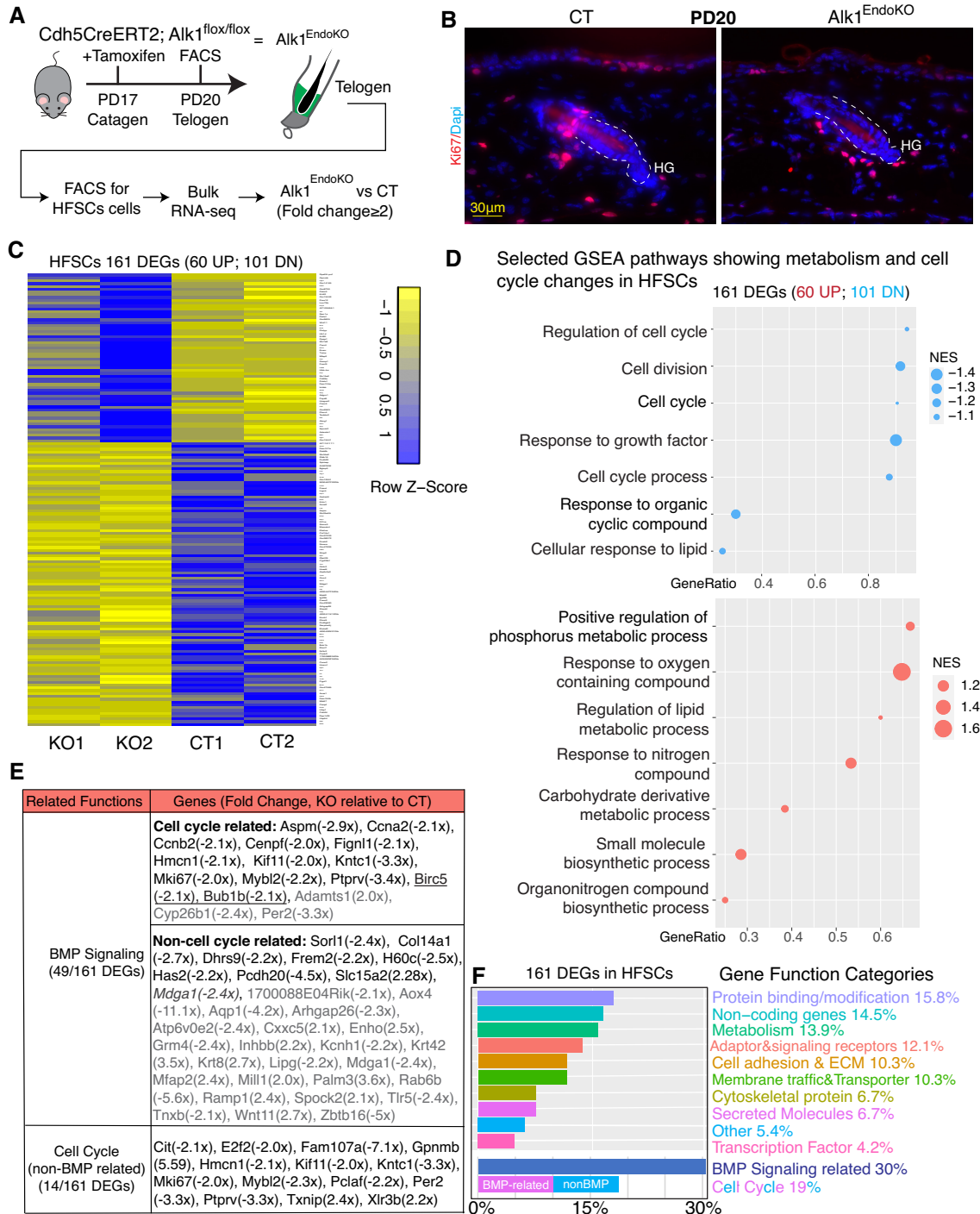


Figure 5.

Alk1 represses BMP4 expression in skin ECs to promote HFSC activation and anagen onset

To test the possibility that BMP signals released from ECs may indeed contribute to the prolonged quiescence of HFSCs, we first confirmed elevated BMP4 expression in the Alk1^{EndoKO} ECs and then performed a rescue experiment by genetic depletion of both BMP4 and Alk1 in the ECs. We tested BMP4 as our main ligand candidate of the BMP

pathway because ECs in other tissues (e.g., lung; Frank David *et al*, 2005) express it, and Alk1^{EndoKO} skin showed elevated BMP4 protein levels (Li *et al*, 2019). We first investigated BMP4 and highly homologous BMP2 mRNA levels in scRNA-seq clusters and observed an increase of BMP4 in the Alk1^{EndoKO} vein cluster and BMP2 in the Alk1^{EndoKO} Capillary 2 cluster (Fig 6A). Immunofluorescence staining with BMP4 antibodies was not reliable when we verified in the Cdh5-CreERT2 × BMP4^{flox/flox} KO mice (BMP4^{EndoKO}). We therefore tested

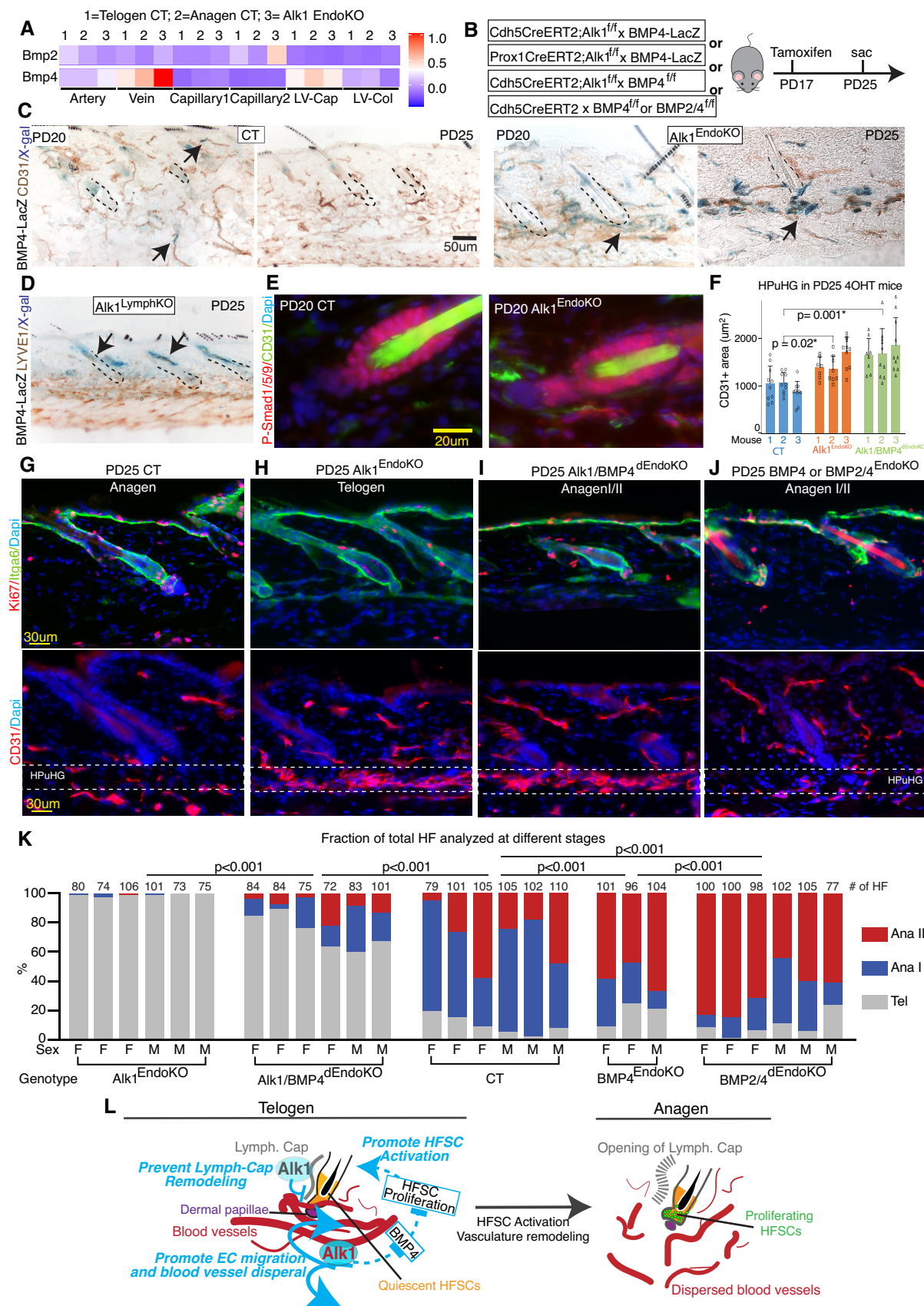


Figure 6.

Figure 6. Alk1 represses BMP4 expression in ECs to promote HFSC activation and anagen onset.

- A BMP2/4 mRNA signal extracted from scRNA-seq data presented in Fig 1. Note specific upregulation of BMP2 in capillary 2 and BMP4 in veins.
- B Schematic showing mouse crosses and the induction timeline.
- C Images of 20 μm skin section of PD20 and PD25 BMP4-LacZ; Alk1f/f; Cdh5-CreERT2 negative, injected with tamoxifen TM at PD17 (labeled as CT), and PD20/PD25 Cdh5CreERT2; Alk1f/f; BMP4-LacZ mice (labeled as Alk1EndoKO) TM injected at PD17, all stained for CD31 (IHC method, brown) and X-gal (blue). Hair follicles (HF) were outlined with black dotted lines. Arrows point to X-Gal+ vascular structure in HPuHG area.
- D Image of 20 μm skin section of PD25 Prox1-CreERT2; Alk1f/f; BMP4-LacZ mice (labeled as Alk1LymphKO) TM injected at PD17, stained for LYVE1 (IHC method, brown) and X-gal (blue). Hair follicles (HF) were outlined with black dotted lines. Arrows point to X-Gal+ vascular structure.
- E Immunofluorescence images 12 μm skin section of PD20 CT and Alk1EndoKO induced at PD17 and stained with p-SMAD1/5/9 (red), CD31 (green), and Dapi (blue).
- F Quantification of HPuHG CD31+ vasculature area in 12 μm skin sections from PD17 induced PD25 CT, Alk1EndoKO, and Alk1 BMP4dKO mice stained for CD31 and Dapi. Error bars represent standard deviation. Each bar represents one individual mouse, and each dot represents measurement from one image. $N = 3$ mice per group, and $n = 7-10$ images per mouse. Restricted maximum likelihood (REML) analysis with unbounded variance components was used as statistical test and individual mouse was treated as random effect to take into the account of mouse-to-mouse variability.
- G–J Immunofluorescence images of 12 μm skin section of PD17 induced stained for (Top panel) Ki67 (red), Itga6 (green), and Dapi (blue) and (Bottom panel) CD31 (red) and Dapi (blue). HPuHG region was outlined with white dotted lines.
- K Quantification of hair follicle percentage of PD17-induced PD25 CT, Alk1EndoKO, Alk1 BMP4dKO, and BMP4EndoKO at telogen, anagen I, and anagen II stages. Telogen hair follicle is defined as no Ki67 in the hair germ. Anagen I is defined as ≤ 7 Ki67+ cells in the unenlarged hair germ. Anagen II is defined as > 7 Ki67+ cells in the hair germ or enlarged hair germ with changed shape that starts to enclose the DP. P -value was generated from Chi-square test. See Table 1 for quantification detail.
- L Model showing Alk1's role in skin vasculature and HFSC activation. In lymphatic vessels (LV), Alk1 works at telogen to repress the widening and fenestration of the lymphatic capillary, a morphology associated with anagen lymphatic capillary, but this is not sufficient to promote normal hair cycle progression. In blood vessels (BV), Alk1 promotes EC migration and BV dispersal from the HPuHG at the transition from telogen to anagen. It also represses BMP4 thus promoting timely HFSC activation in hair cycle.

BMP4 expression in the skin via the BMP4-LacZ knock-in reporter mice previously generated (Lawson *et al.*, 1999; Fig 6B). We crossed the Alk1^{EndoCT/KO} mice with the BMP4-LacZ knock-in reporter mice and found that CT mice (Cre negative, TM injected) littermates showed little if any X-Gal signal in the skin at both stages examined (PD20 and 25, telogen and early anagen, respectively), while PD25 Alk1^{EndoKO} mice showed strong X-gal signal co-localizing with a fraction of the CD31+ skin vascular structures; this signal increase was in fact already apparent at PD20 in the Alk1^{EndoKO} skin (Fig 6C) and was never detected to this extent in any CT samples. Interestingly, our CT mice did not show LacZ expression in the dermal papillae as we observed in the original BMP4-LacZ strain and was also reported by (Plikus *et al.*, 2008). We also crossed the BMP4-LacZ mice with our Alk1^{LymphKO} and found co-localization between X-gal signal with lymphatic vessels when co-stained with LYVE1 antibody (Fig 6D). These data suggest that Alk1 loss in ECs promotes BMP4 expression in CT skin ECs, corroborating our transcriptomic data that indicate some BMP signaling target genes were elevated in HFSCs (Fig 5E and F). To test the strength of BMP signaling in HFSCs, we stained PD20 skin with P-Smad1/5/9 antibodies. Interestingly, the CD31-stained vasculature in the Alk1^{EndoKO} skin shows P-Smad1/5/9-associated signal, consistent with increased BMP4 production from the vasculature, while CT HFSCs showed P-Smad signal only in the bulge and sometimes in hair germ, as previously reported (Genander *et al.*, 2014; Fig 6E). Despite multiple experiments and several mice analyzed per group, an obvious increase in SMAD1/5/9 activation in the HFs of the Alk1^{EndoKO} skin was not apparent in this approach (Fig 6E), and hence, the data are presented qualitatively here. This may not be surprising given negative feedbacks were reported in the BMP pathway upon transient overactivation that carries on transcription of downstream target genes (Economou & Hill, 2020). Interestingly, *Inhbb*, a BMP antagonist (Wiater & Vale, 2003), was already upregulated along with other BMP target genes in the HFSCs of the Alk1^{EndoKO} skin by PD20, suggesting possible initiation of a negative feedback loop that may dampen a transient overactivation of the pathway. Moreover, it has been proposed that sustained (rather than

net increase in) BMP signaling strength as measured by P-Smad levels may promote robust gene expression changes of BMP downstream target genes (Economou & Hill, 2020).

To definitively test if high BMP4 expression from the Alk1^{EndoKO} ECs contributes to the HFSC activation delay in these mice, we designed a genetic rescue experiment. We crossed the Cdh5-CreERT2; Alk1^{flox/flox} mice with BMP4^{flox/flox} mice (Liu *et al.*, 2004) to generate pan-EC specific Alk1/BMP4 double KO mice (Alk1/BMP4^{dEndoKO}). To prolong their lifespan after knockout, instead of TM injections, we induced the mice with topical application of 4-Hydroxytamoxifen (4OHT) at PD17. We first verified the high efficiency of this induction scheme with Rosa26R-lox-STOP-lox-tdTomato reporter mice (Fig EV5E–G). Then we showed that Alk1^{EndoKO} mice topically induced with 4OHT displayed both the dense HPuHG and the delayed HFSC activation relative to Cre-negative CT mice (Fig 6F–H), as expected from our previous experiments with TM injection. The Alk1/BMP4^{dEndoKO} mice displayed a dense HPuHG when compared with CT mice, which was indistinguishable from the Alk1^{EndoKO} mice (Fig 6G–I bottom panels and quantified in 6F). This suggests that BMP4 depletion in ECs does not rescue the vasculature remodeling defect induced by the Alk1^{EndoKO}, maintaining the abnormally dense HPuHG. In contrast, HFSC activation in the Alk1/BMP4^{dEndoKO} was intermediate between CT and Alk1^{EndoKO} mice, as judged by Ki67 staining of skin sections (Fig 6G–I top panels and mice summarized in 6K and Table 1). This demonstrates that BMP4 loss in ECs partially rescues the HFSC activation defect induced by Alk1 loss in ECs. Finally, mice with EC deletion of BMP4 alone (Cdh5-CreERT2xBMP4^{flox/flox} = BMP4^{dEndoKO}) and with BMP2/4 double deletion (BMP2/4^{dEndoKO}) showed mild acceleration in HFSC activation or hair cycle progression, notable at the early time point of analysis (PD25; Figs 6J and K, and EV5H–J). The HPuHG area also appeared normal in the BMP4^{dEndoKO} mice upon inspection in microscopy analysis (Fig 6J) and was not further quantitatively analyzed here. Given the sporadic frequency and low expression of BMP4 in normal WT skin ECs as indicated by the BMP-LacZ data (Fig 6C, left), the lack of apparent phenotype in vasculature upon BMP ligand loss may not be

surprising although this loss was sufficient to mildly accelerate the hair cycle.

In conclusion, our genetic rescue experiments here show that *Alk1* loss perturbs the BV spatial organization around the lower hair follicle in the HPuHG and elevates BMP4 expression in the ECs; this vascular perturbation is maintained in the context of simultaneous *Alk1/BMP4* loss in ECs, while the HFSC activation delay is partially alleviated in this context. Furthermore, BMP4 and BMP2/4 genetic depletion from the ECs mildly accelerates HFSC activation. These results demonstrate that in regulating the hair follicle homeostatic cycle, *Alk1* represses BMP4 in ECs, thus ensuring timely activation of HFSCs from quiescence during hair cycle in a non-cell-autonomous manner (Fig 6L).

Discussion

Skin endothelial cells (ECs) have recently emerged as putative tissue niches for the activation of HFSCs (Fuchs *et al*, 2004; Tumber, 2012; Li & Tumber, 2021), but to date molecular signals flowing from ECs have not been directly demonstrated to regulate HFSCs. Furthermore, whereas lymphatic vessels (LVs) ablation indicates that this skin EC compartment influences HFSC activation (Gur-Cohen *et al*, 2019; Peña-Jimenez *et al*, 2019), the role for blood vessels (BVs) ECs in the molecular cross-talking with HFSCs was unclear until now. BV ECs are especially interesting to study in highly regenerative tissues such as the skin as they can, in theory, coordinate two essential needs: (i) supply O₂ and nutrients to provide energy and (ii) stimulate SCs to produce more tissue building blocks. Overall, our work here implicates a novel *Alk1-BMP4* signaling axis in BV ECs that regulates adult HFSC activation and hair cycle progression (Fig 6L). This adds another tissue system to the list of SCs to which EC signal during adult homeostasis (Ramasamy *et al*, 2015; Comazzetto *et al*, 2021). We suggest that skin blood vessels act on hair follicle stem cell quiescence via paracrine signaling, a function that is modulated by *Alk1*, which suppresses quiescence signals from the vasculature, thus promoting HFSC activation.

Importantly, we show here that genetic depletion of *Alk1*, a well-known vasculature regulator, in both BV and LV ECs but not in LVs alone, inhibits HFSC activation. This demonstrates an important role of blood vessels in hair cycle and HFSC regulation. *Alk1* depletion in LVs alone accelerates the hair cycle-associated remodeling of skin lymphatic capillary promoting a premature anagen-like morphology, while the hair follicle itself remains behind in the hair cycle. Taken together with previous LV ablation experiment (Gur-Cohen *et al*, 2019; Peña-Jimenez *et al*, 2019), this result suggests that the LV remodeling itself may be insufficient for driving normal progression of the hair cycle. One possibility is that molecular signals from LVs together with changes in LV capillary morphology (Gur-Cohen *et al*, 2019; Peña-Jimenez *et al*, 2019) may drive hair cycle. Intriguingly, recent work suggested that *Sostdc1*, a BMP antagonist, is secreted by the LVs (Yoon & Detmar, 2022), although the relevance of this molecule to HFSCs has not yet been tested.

Importantly, we find that *Alk1* normally acts in ECs to inhibit BMP4, a ligand of the BMP-signaling pathway, well-known to promote HFSC (Botchkarev & Sharov, 2004; Plikus *et al*, 2008; Lee & Tumber, 2012). Our work utilizing BMP4-LacZ reporter mice demonstrates that BMP4 is expressed weakly and sporadically in ECs in

the HPuHG area, but is strongly upregulated in skin vasculature upon *Alk1* loss, confirming our previous analysis (Li *et al*, 2019). This, together with the crowding of BVs near the hair germ upon *Alk1* loss in ECs (Li *et al*, 2019 and this work), likely creates a proliferative inhibitory environment for the HFSCs (Fig 6L). Importantly, our genetic depletion of BMP4 in ECs rescues in part the HFSC activation defect induced by *Alk1* loss, while leaving the dense vasculature defect intact. Furthermore, BMP4 and BMP2/4 genetic depletion from the ECs that are WT for *Alk1* also promotes HFSC activation, albeit mildly. The caveat of a potential systemic effect of *Alk1* loss notwithstanding, these results collectively place BMP ligands as the first identified EC secreted signals, capable to inhibit HFSC activation and to regulate hair cycle progression in a non-cell-autonomous manner. In the future, it would be worth investigating the long-term rescue effect of BMP4 in the *Alk1* knockout, potentially through mosaic knockout induction to avoid the lethality issue and any potential systemic effects. Overall, this work uncovers the *Alk1-BMP* signaling axis in skin ECs acting in HF homeostasis to create a proper environment for normal HFSC activity, coordinating the HFSC timely activation with proper skin vascular remodeling during hair cycle (Fig 6L).

Our results suggest that the increased BMP signals from ECs may act directly on HFSCs, which are known to express the BMPRI receptor and respond to BMP signals by maintaining quiescence (Botchkarev & Sharov, 2004; Plikus *et al*, 2008; Lee & Tumber, 2012). With that said, we cannot formally exclude that other signaling pathways and other skin compartments may also play an intermediary role in the communication of vasculature with HFSCs. In fact, *Alk1* may directly or indirectly regulate expression of many genes important for EC metabolism, cell adhesion, and various other cellular functions in ECs, as suggested by our transcriptomic data. Considering the function of the skin vasculature to bring various metabolites to HFSCs and the fact that other non-endothelial cell types also secrete BMPs in the skin (Botchkarev & Sharov, 2004; Plikus *et al*, 2008; Lee & Tumber, 2012), it is very possible that the *Alk1*-null ECs are not able to fully support vascular function, explaining why the HFSC activation delay is only partially rescued in the *Alk1/BMP4* double KO.

BV ECs seem to have a broad angiocrine function in tissue morphogenesis and adult stem cell regulation, where they employ tissue-specific signals resulting from plasticity in response to local microenvironments (Ramasamy *et al*, 2015). With that said, BMP signaling to neighboring stem/progenitor cells is not restricted to skin ECs downstream of *Alk1* (this work) but was also found in the dorsal aorta where it controls segregation of neuro-progenitors and in lung stem cell differentiation during pulmonary regeneration from injury (Ramasamy *et al*, 2015). Thus, BMP may work more ubiquitously in BV ECs than previously recognized.

Finally, while the role of *Alk1* in vascular remodeling during development and in response to injury or pathological conditions has been well described (Oh *et al*, 2000; Seki *et al*, 2003; Park *et al*, 2009; Roman & Hinck, 2017), we just began to uncover *Alk1*'s role in vasculature remodeling during adult homeostasis, specifically in the hair cycle (Li *et al*, 2019 and this work). While all skin EC compartments are affected by *Alk1* loss, EC proliferation previously observed upon *Alk1* loss in the retina and in ECs *in vitro* (Scharpfenecker *et al*, 2007; Tual-Chalot *et al*, 2014; Alsina-Sanchis *et al*, 2018), was not affected in the skin. In fact, our results point strongly

to Alk1 possible role in EC mobilization/migration from the HPuHG area at the telogen–anagen transition, as Alk1^{EndoKO} mice abandoned the well-documented spatial remodeling of vasculature that occurs in WT mice at this stage. Our interpretation is in line with Alk1's well-known role in skin EC migration in cell culture and in other tissue systems (Rochon *et al*, 2016; Park *et al*, 2021). Similarly, in Zebrafish, Alk1 loss does not alter ECs proliferation but promotes EC migration with the direction of blood flow (Rochon *et al*, 2016). This abnormal flow–migration coupling is thought to drive arteriovenous malformations (AVM; Park *et al*, 2021), the fusions of arteries and veins, which is a major symptom of a human disease known as hereditary hemorrhagic telangiectasia (HHT; Tual-Chalot *et al*, 2014; Ruiz-Llorente *et al*, 2017). Interestingly, we find that tortuous vasculature, which may precede AVM, form upon Alk1 loss in the absence of skin injury, as part of the perturbed remodeling of skin vasculature in the HPuHG during hair cycle. It is also worth noting that BMP4's established role in ECs includes promoting sprouting angiogenesis and increasing vascular permeability (Heinke *et al*, 2008; Dyer *et al*, 2014; Helbing *et al*, 2017), which corroborate with the phenotype we observed in Alk1^{EndoKO}. Therefore, the Alk1-BMP signaling axis may have both a cell non-autonomous role in HFSC and a cell-autonomous role in ECs to regulate skin homeostasis.

In closing, our work uncovers the first instance of blood endothelial cells acting as skin signaling niches in adult homeostasis, where these cells employ an Alk1-BMP axis to ensure proper timing of hair follicle stem cell activation during hair cycle in a cell non-autonomous manner.

Materials and Methods

Mice and treatments

All mouse work was compliant with the Cornell University Institutional Animal Care and Use Committee (IACUC) guidelines (protocol number no. 2007-0125). Cdh5CreERT2 (Sørensen *et al*, 2009) × Alk1^{flox/flox} (Mixed background of C57BL/6, 129, and 129/SvJae; Park *et al*, 2008) mice were imported from Dr. Anne Eichmann at Yale University. BMP2^{flox/flox} (Ma & Martin, 2005) and BMP4^{flox/flox} (Liu *et al*, 2004) mice were imported from Dr. Jian Q. Feng at Texas A&M University. BMP4-LacZ (C57BL/6; Lawson *et al*, 1999) mice were imported from Dr. Jan L. Christian at University of Utah. Prox1-CreERT2 (Prox1^{tm3(cre/ERT2)Gco}) mice (Srinivasan *et al*, 2007), Rosa26R-lox-STOP-lox-tdTomato (Madisen *et al*, 2010) mice were purchased from Jackson Laboratory. We crossed Prox1-CreERT2 mice with Alk1^{flox/flox} mice to generate the Alk1^{LymphKO} mice. Primers used for genotyping are in Appendix Table S1.

To induce Prox1-CreERT2 activity, Alk1^{LymphKO} mice were injected with 200 µg/g of body weight of tamoxifen (Sigma) in oil through intraperitoneal (IP) injection. To induce Cdh5-CreERT2 activity, 100 µg/g of body weight of tamoxifen in oil was injected through IP. For BrdU-pulse experiments, mice were fed with 0.8 mg/ml BrdU in daily water supply. For 4OHT treatment, we dissolved 4-hydroxy-tamoxifen (Sigma, H-7904) in a 1:1 solution of Ethanol and Cremphor (Sigma, C5135) to make the 20 mg/ml stock. Then dilute the stock with PBS to make a 2 µg/µl working solution. Mice were anesthetized with isoflurane. Their back skin was shaved

but not close to the skin to avoid triggering unwanted hair growth. 80 µl of the 4OHT working solution was applied to the back skin per mouse.

Cre-negative littermates injected with tamoxifen were used as control in all studies involving control and knockout except our single-cell RNA-seq experiment where non-littermates were used. Samples without tdTomato were collected by directly embedding in Optimal Cutting Temperature (OCT) compound (Tissue Tek, Sakura) on dry ice. Samples with tdTomato were prefixed in 4% Paraformaldehyde solution for 4 h in 4°C and incubated in 15% sucrose and 30% sucrose solution overnight. Then samples were washed in PBS and embedded in OCT compound.

Immunofluorescent staining

Immunofluorescent staining was performed following a standard protocol, as described previously (Scheitz *et al*, 2012; Lee *et al*, 2014; Li *et al*, 2019). In brief, OCT-embedded samples were cryosectioned and collected on slides. Then they were fixed in 4% paraformaldehyde solution (PFA) for 10 min at room temperature. After washing with PBS, tissue sections were blocked in 5% normal serum solution and incubated with primary antibodies overnight at 4°C. After washing, tissue sections were incubated with corresponding Alexa488/568/594-, FITC-, and Cy5-conjugated secondary antibodies against IgG of animals where primary antibodies were raised, and Dapi for 1 h at room temperature. Slides were mounted with antifade and stored in –20°C before imaging.

For BrdU staining, tissue sections were first stained for other non-BrdU primary antibodies following the standard protocol described above. Then slides were fixed in 4% PFA and incubated in 1 M HCl solution for 55 min at 37°C plus 5 min in ice bath. After washing with PBS, slides were blocked in 0.5% Tween-20 and 1% BSA and incubated with anti-BrdU antibody overnight at 4°C. Then slides were washed in PBS and incubated with FITC-conjugated anti-Rat antibody and Dapi for 1 h at room temperature. Slides were mounted with antifade and stored in –20°C before imaging.

Primary antibodies used in this study include CD31 (1:100, BD Biosciences, 5502741); Cdh5 (1:500, R&D Systems, AF1002); VEGFR3 (1:400, R&D Systems, AF743); LYVE1 (1:400, Thermo Scientific, 14-0443-82); Erg (1:300, Abcam, ab92513); Prox1 (1:300, Abcam, ab199359); Ki67 (1:1,000, Abcam, 15580); BrdU (1:300, Abcam ab6326); Keratin14 (1:2,000, Covance, PRB-155P); Integrin alpha6 (1:1,000, R&D Systems, MAB13501); P-SMAD1/5/8 (1:300, Cell Signaling Technology, 13820S); Endomucin (1:300, Santa Cruz Biotechnology, sc-65495); CD34 (1:100, BD Biosciences, 550274).

Whole mount staining

Mice were sacrificed and hair was removed using hair removal cream (Nair). Skin was then washed in PBS to remove excess cream and trimmed into 2–5 mm² pieces. After fixing in 4% PFA at 4°C for 4 h, skin pieces were permeabilized in blocking buffer (0.1% Triton, 2% serum, and 0.2% sodium azide in PBS) overnight and incubated with primary antibody diluted in blocking buffer for 2 days at 4°C. Then skin pieces were washed in PBS overnight at 4°C. Then they were incubated with secondary antibody and Dapi diluted in PBST (0.1% Triton and 0.2% sodium azide in PBS) for 2 days at 4°C, followed by another overnight incubation in PBS at 4°C. Skin pieces

were then washed for 1 h incubation each through an ethanol gradient from 50, 70, 100%, and another 100% to dehydrate at room temperature. They were then incubated with ethyl cinnamate (Sigma-Aldrich, 112372-100G) for 1 h at room temperature for clearing. All incubations were performed on a rocker. Antibody dilutions are the same for whole mount staining and standard immunofluorescence staining.

Microscopy and image quantification

Immunofluorescent staining images from 8 and 12 μm sections and sorted cells were captured with Leica DMI6000B microscope and Leica K5 camera. Images were processed and enhanced for brightness and contrast using FIJI (Schindelin et al, 2012). All quantifications were performed using FIJI. For image quantifications, HPuHG region was defined as a 30 μm region below the hair germ (Li et al, 2019). HPuHG vasculature was defined as vasculatures within the 30 μm region as well as those extending below the region. Vasculature area was measured using the Freehand Selections tool in FIJI by manually outlining the immunoreactive area. For hair cycle quantification, upper back skin is used in all mice for consistency. Telogen hair follicle is defined as no Ki67 in the hair germ. Anagen I is defined as ≤ 7 Ki67+ cells in the unenlarged hair germ. Anagen II is defined as > 7 Ki67+ cells in the hair germ or enlarged hair germ with changed shape that starts to enclose the DP. For quantification of induction efficiency of Prox1-CreERT2; Rosa26R-lox-STOP-lox-tdTomato, tdTomato+ area and VEGFR3+ area were manually outlined, and areas were measured. The induction efficiency is calculated as the ratio of tdTomato+ area to VEGFR3+ area. For quantification of induction efficiency of Cdh5-CreERT2; Rosa26R-lox-STOP-lox-tdTomato, tdTomato+ area and VEGFR3+ area were manually outlined, and areas were measured. The induction efficiency is calculated as the ratio of tdTomato+ area to CD31+ area. For the quantification of lymphatic capillary width, the Lyve1+ area of each lymphatic capillary was first measured by manually circling the Lyve+ area using the Freehand Selections tool. Then the side length (hair follicle side) of the lymphatic capillary was measured using the Freehand Line tool. Lymphatic capillary width was calculated as the lymphatic capillary area divided by the side length of the lymphatic capillary (Fig EV4H). Figure were generated using GraphPad Prism 8.

Immunofluorescent staining images from 60 μm thick sections (used for lymphatic capillary width quantification) were captured using the Zeiss LSM upright or inverted 880 confocal microscope and 40 \times LD or non-LD C-Apochromat lens. Pinhole was set to 1 Airy Unit, and z-step was 1 μm between each single optical plane. Images were processed using Zen software (Zeiss) for stitching and maximum intensity projections and quantified using FIJI.

Whole mount samples were imaged using the Zeiss LSM upright 880 confocal microscope and the 40 \times LD C-Apochromat lens. Pinhole was set to 1 Airy Unit, and z-step was 2 μm between each single optical plane. Images were processed using Imaris (Bitplane) for volume rendering and movie generation.

Fluorescence activated cell sorting

FACS isolation of endothelial cells was performed as described previously (Chovatiya et al, 2021). For sorting of tdTomato+ ECs,

Cdh5-CreERT2 (Sørensen et al, 2009) and Rosa26R-lox-STOP-lox-tdTomato (Jax Stock #007905) with and without Alk1^{floxed/floxed} allele (CT and Alk1^{EndoKO} respectively) were used for EC isolation. The mice are injected with 100 $\mu\text{g/g}$ of Tamoxifen at PD17, and dorsal skin was collected at PD20 and PD32 for CT mice, and at PD25 for Alk1^{EndoKO} mice. The dorsal skin was digested in collagenase and dispase as described (Chovatiya et al, 2021). Dead cells were excluded using LIVE/DEAD™ Fixable Aqua Dead Cell Stain Kit (ThermoFisher). tdTomato+ cells were sorted as ECs.

Bulge HFSCs were sorted as described previously (Waghmare et al, 2008). Briefly, dorsal skin of PD20 CT mice and Alk1^{EndoKO} mice induced on PD17 were collected. The epidermis was scrapped and digested in trypsin. Single cells were labeled with CD34-Biotin (eBioscience, 13-0341-85), PE-Cd49f (Itga6; BD Biosciences, 555736) as primary antibodies, and APC-Streptavidin (BD Biosciences, 554067) as secondary antibody. Dead cells were excluded using Dapi, and HFSCs were purified based on PE and APC intensity (CD34+ Itga6+), which gives $> 95\%$ enrichment in HFSCs (Waghmare et al, 2008). BD Aria (BD Biosciences) and MA900 (SONY) were used for sorting.

Single-cell library preparation and data analysis

Single-cell 3' cDNA libraries were prepared from Chromium Single Cell 3' gel bead and library Kit v3 (10 \times Genomics) and sequenced using an Illumina NextSeq-500. The raw data were aligned to the mouse reference genome (mm10-2020-A) using the 10 \times Genomics Cell Ranger pipeline (v6.0.1). The filtered_feature_bc_matrix files were then analyzed in R using Seurat 4.0 (Hao et al, 2021). As described in Chovatiya et al (2021), cells detected to express 200–5,000 genes and have less than 10% of the UMIs mapped to mitochondrial genes were retained. All samples were then merged, and read counts were normalized. Data integration was done through Principal Component Analysis (PCA) embeddings using Harmony (Korsunsky et al, 2019). Non-endothelial cells were removed based on marker expressions (Fig EV2E). Retained endothelial cells were re-clustered and assigned with corresponding identity. A list of 1,722 differentially expressed genes for each endothelial cluster in CT and Alk1^{EndoKO} samples was generated using the FindMarkers in Seurat with log2 fold change cutoff of > 0.5 . These 1,722 DEGs were categorized into different biological processes using the Panther database (Mi et al, 2019, 2021). Gene Ontology analysis was performed on GSEA software with the list of differentially expressed genes using software default setting and classic enrichment statistics (Mootha et al, 2003; Subramanian et al, 2005). Enriched gene sets were then loaded into Rstudio for plotting. Pathway scoring analysis was performed by loading the gene list of the GO term and using the AddModule function in Seurat to calculate the pathway score.

RNA-seq library preparation and data analysis

Total RNAs were isolated from sorted skin cells prepared by TriZol method provided by Cornell TReX facility (version 1.8). Briefly, cells were directly sorted to TriZol. Then 0.2 ml of chloroform was added to 1 ml of TriZol lysate followed by centrifuge. GlycoBlue coprecipitant (Invitrogen, AM9515) was added to the aqueous phase, which was then transferred to a new tube with isopropanol and incubated for 30 min at room temperature, followed by centrifugation. Then

the RNA pellet was washed with 75% ethanol twice and redissolved in nuclease free water.

Isolated RNA was then sent to a Fragment Analyzer (Advanced Analytical) to determine the RNA integrity. RNA with RQN > 7 was submitted for RNA-seq libraries preparation at the Cornell TREX facility.

RNA-seq library was prepared using NEBNext Ultra II Directional RNA Library Prep Kit (New England Biolabs) with PolyA enrichment as per NEB protocol and sequenced on a NovaSeq (Illumina), S4 flowcell at Novogene. Initial data processing and analysis were done as in Cornell TREX RNA-seq methods V2 (Ghuwalewala *et al*, 2022). Briefly, reads were trimmed to remove low quality and adaptor sequences with *TrimGalore* v0.6.0 (Krueger *et al*, 2021), a wrapper for *cutadapt* (Martin, 2011) and *fastQC* (Andrews *et al*, 2012). The unwanted reads were subtracted, and the remaining reads were mapped to the GRCm38 genome using *STAR* v 2.7.0e (Dobin *et al*, 2013). Gene expression analysis was done using *SARTools* and *DESeq2* v1.26.0 to generate normalized counts and statistical analysis of differential gene expression (Love *et al*, 2014).

The gene list generated from the above analysis was then filtered for criteria mentioned in the main text, including (i) minimum read count of 50 in at least one sample, (ii) average twofold change between CT and *Alk1*^{EndoKO} HFSCs, and (iii) consistent DEG changes in each pair of CT versus *Alk1*^{EndoKO} mice. This stringent list of 161 DEGs was used for subsequent analysis. Gene Ontology analysis was performed using GSEA software (Mootha *et al*, 2003; Subramanian *et al*, 2005). Pathways with NES > 1 were plotted. Classification of gene category was based on Panther Database (Mi *et al*, 2019, 2021), GeneCards (RRID:SCR_002773), and literature.

Statistical analysis and data reproducibility

All experiments were performed at least twice. For staining, at least three mice were used for each group with at least three technical replicates per mouse. For image data used for quantifications, at least eight images were analyzed for each mouse. Statistical tests were performed using JMP Pro 15 and graphed as mean with standard deviation. Restricted maximum likelihood (REML) analysis with unbounded variance components was used as statistical test for most quantifications comparing control and knockout mice. Individual mouse was treated as random effect to take into the account of mouse-to-mouse variability. For Fig 2H, we used unpaired two-tailed student *t*-test. For Fig 6K, we performed Chi-square test. Significant difference was defined as *P*-value < 0.05.

Data availability

The scRNA-seq data have been deposited in the Gene Expression Omnibus (GEO) database with accession code: GSE211381 (<https://www.ncbi.nlm.nih.gov/geo/query/acc.cgi?acc=GSE211381>). Bulk RNA data have been deposited in the GEO database with accession codes: GSE223723 (<https://www.ncbi.nlm.nih.gov/geo/query/acc.cgi?acc=GSE223723>). All other data are available on request from the corresponding author.

Expanded View for this article is available [online](#).

Acknowledgments

We thank L. Tesfa and J. E. Mahoney for FACS; C. J. Bayles, R. M. Williams, and J. M. Dela Cruz for confocal imaging (BRC Facility, NYSTEM C029155, and NIH S100D018516); J. Grenier, A. E. Tate, and F. Ahmed for RNA sequencing (TREX facility); P. A. Schweitzer for 10X Genomics scRNA-seq run; the Cornell CARE staff for mouse husbandry; the Cornell Statistical Consulting Unit for statistical consultation. We also thank Dr. Anne Eichmann at Yale University for sharing the *Alk1*^{flox/flox} × *Cdh5-CreERT2* mice, Dr. Jian Q. Feng at Texas A&M University for sharing the *BMP2*^{flox/flox} and *BMP4*^{flox/flox} mice, and Dr. Jan L. Christian at University of Utah for sharing the *BMP4-LacZ* mice. The research was supported by grants from the National Institute of Arthritis and Musculoskeletal and Skin Diseases (R01AR070157 and R01AR073806 and R56AR081021) to T.T. GC was partially supported by a training grant from the Empire State Stem Cell Fund through New York State Department of Health Contract # C30293GG. Opinions expressed here are solely those of the author and do not necessarily reflect those of the Empire State Stem Cell Board, the New York State Department of Health, or the State of New York.

Author contributions

Kefei Nina Li: Conceptualization; data curation; software; formal analysis; validation; investigation; visualization; methodology; writing – original draft; writing – review and editing. **Gopal Chovatya:** scRNAseq of CT mice at telogen and anagen; data curation; software; investigation; visualization; methodology; writing – review and editing. **Daniel Youngjoo Ko:** Formal analysis; validation; investigation; visualization. **Sripad Sureshbabu:** Validation; investigation; visualization. **Tudorita Tumar:** Conceptualization; resources; supervision; funding acquisition; investigation; methodology; writing – original draft; project administration; writing – review and editing.

Disclosure and competing interests statement

T.T. is member of the EMBO Journal editorial advisory board.

References

- Alsina-Sanchis E, García-Ibáñez Y, Figueiredo Ana M, Riera-Domingo C, Figueras A, Matias-Guiu X, Casanovas O, Botella Luisa M, Pujana Miquel A, Riera-Mestre A *et al* (2018) ALK1 loss results in vascular hyperplasia in mice and humans through PI3K activation. *Arterioscler Thromb Vasc Biol* 38: 1216–1229
- Andrews S, Krueger F, Segonds-Pichon A, Biggins L, Krueger C, Wingett S (2012) FastQC: a quality control tool for high throughput sequence data <https://www.bioinformatics.babraham.ac.uk/projects/fastqc>
- Botchkarev VA, Sharov AA (2004) BMP signaling in the control of skin development and hair follicle growth. *Differentiation* 72: 512–526
- Bühler A, Berger S, Bengsch F, Martin G, Han H, Vierkotten S, Pielen A, Boehringer D, Schlunck G, Fauser S *et al* (2013) Cathepsin proteases promote angiogenic sprouting and laser-induced choroidal neovascularisation in mice. *Exp Eye Res* 115: 73–78
- Chase HB, Montagna W, Malone JD (1953) Changes in the skin in relation to the hair growth cycle. *Anat Rec* 116: 75–81
- Chovatya G, Ghuwalewala S, Walter LD, Cosgrove BD, Tumar T (2021) High-resolution single-cell transcriptomics reveals heterogeneity of self-renewing hair follicle stem cells. *Exp Dermatol* 30: 457–471
- Chovatya G, Li KN, Ghuwalewala S, Tumar T (2023) Single-cell transcriptomics of adult skin VE-cadherin expressing lineages during hair cycle. *bioRxiv* <https://doi.org/10.1101/2023.03.22.533784> [PREPRINT]

- Comazzetto S, Shen B, Morrison SJ (2021) Niches that regulate stem cells and hematopoiesis in adult bone marrow. *Dev Cell* 56: 1848–1860
- Cotsarelis G (2006) Epithelial stem cells: a Folliculocentric view. *J Invest Dermatol* 126: 1459–1468
- Dobin A, Davis CA, Schlesinger F, Drenkow J, Zaleski C, Jha S, Batut P, Chaisson M, Gingeras TR (2013) STAR: ultrafast universal RNA-seq aligner. *Bioinformatics* 29: 15–21
- Durward A, Rudall KM (1958) CHAPTER 9 - the vascularity and patterns of growth of hair follicles. In *The biology of hair growth*, Montagna W, Ellis RA (eds), pp 189–218. New York, NY: Academic Press
- Dyer LA, Pi X, Patterson C (2014) The role of BMPs in endothelial cell function and dysfunction. *Trends Endocrinol Metab* 25: 472–480
- Economou AD, Hill CS (2020) Chapter twelve - temporal dynamics in the formation and interpretation of nodal and BMP morphogen gradients. In *Current topics in developmental biology*, Small S, Briscoe J (eds), pp 363–389. New York, NY: Academic Press
- Eto N, Miyagishi M, Inagi R, Fujita T, Nangaku M (2009) Mitogen-activated protein 3 kinase 6 mediates angiogenic and tumorigenic effects via vascular endothelial growth factor expression. *Am J Pathol* 174: 1553–1563
- Frank David B, Abtahi A, Yamaguchi DJ, Manning S, Shyr Y, Pozzi A, Baldwin HS, Johnson Joyce E, de Caestecker MP (2005) Bone morphogenetic protein 4 promotes pulmonary vascular remodeling in hypoxic pulmonary hypertension. *Circ Res* 97: 496–504
- Fuchs E, Tumber T, Guasch G (2004) Socializing with the neighbors: stem cells and their niche. *Cell* 116: 769–778
- Genander M, Cook PJ, Ramsköld D, Keyes BE, Mertz AF, Sandberg R, Fuchs E (2014) BMP signaling and its pSMAD1/5 target genes differentially regulate hair follicle stem cell lineages. *Cell Stem Cell* 15: 619–633
- Ghuwalewala S, Lee SA, Jiang K, Baidya J, Chovatiya G, Kaur P, Shalloway D, Tumber T (2022) Binary organization of epidermal basal domains highlights robustness to environmental exposure. *EMBO J* 41: e110488
- Gur-Cohen S, Yang H, Baksh SC, Miao Y, Levorse J, Kataru RP, Liu X, de la Cruz-Racelis J, Mehrara BJ, Fuchs E (2019) Stem cell-driven lymphatic remodeling coordinates tissue regeneration. *Science* 366: 1218–1225
- Haase N, Rüder C, Haase H, Kamann S, Kouno M, Morano I, Dechend R, Zohlnhöfer D, Haase T (2017) Protective function of Ahnak1 in vascular healing after wire injury. *J Vasc Res* 54: 131–142
- Hao Y, Hao S, Andersen-Nissen E, Mauck WM III, Zheng S, Butler A, Lee MJ, Wilk AJ, Darby C, Zager M et al (2021) Integrated analysis of multimodal single-cell data. *Cell* 184: 3573–3587.e29
- Heinke J, Wehofsits L, Zhou Q, Zoeller C, Baar K-M, Helbing T, Laib A, Augustin H, Bode C, Patterson C et al (2008) BMPER is an endothelial cell regulator and controls bone morphogenetic protein-4-dependent angiogenesis. *Circ Res* 103: 804–812
- Helbing T, Wiltgen G, Hornstein A, Brauers EZ, Arnold L, Bauer A, Esser JS, Diehl P, Grundmann S, Fink K et al (2017) Bone morphogenetic protein-modulator BMPER regulates endothelial barrier function. *Inflammation* 40: 442–453
- Houschyar KS, Borrelli MR, Tapking C, Popp D, Puladi B, Ooms M, Chelliah MP, Rein S, Pförringer D, Thor D et al (2020) Molecular mechanisms of hair growth and regeneration: current understanding and novel paradigms. *Dermatology* 236: 271–280
- Hsu Y-C, Li L, Fuchs E (2014) Transit-amplifying cells orchestrate stem cell activity and tissue regeneration. *Cell* 157: 935–949
- Korsunsky I, Millard N, Fan J, Slowikowski K, Zhang F, Wei K, Baglaenko Y, Brenner M, Loh P-r, Raychaudhuri S (2019) Fast, sensitive and accurate integration of single-cell data with harmony. *Nat Methods* 16: 1289–1296
- Krueger F, James F, Ewels P, Afyounian E, Schuster-Boeckler B (2021) FelixKrueger/TrimGalore: v0.6.7 - DOI via Zenodo. Zenodo <https://doi.org/10.5281/zenodo.5127899>
- Larrivée B, Prahst C, Gordon E, del Toro R, Mathivet T, Duarte A, Simons M, Eichmann A (2012) ALK1 signaling inhibits angiogenesis by cooperating with the notch pathway. *Dev Cell* 22: 489–500
- Lawson KA, Dunn NR, Roelen BA, Zeinstra LM, Davis AM, Wright CV, Korving JP, Hogan BL (1999) Bmp4 is required for the generation of primordial germ cells in the mouse embryo. *Genes Dev* 13: 424–436
- Lee J, Tumber T (2012) Hairy tale of signaling in hair follicle development and cycling. *Semin Cell Dev Biol* 23: 906–916
- Lee SE, Sada A, Zhang M, McDermitt David J, Lu Shu Y, Kempthues Kenneth J, Tumber T (2014) High Runx1 levels promote a reversible, more-differentiated cell state in hair-follicle stem cells during quiescence. *Cell Rep* 6: 499–513
- Li KN, Tumber T (2021) Hair follicle stem cells as a skin-organizing signaling center during adult homeostasis. *EMBO J* 40: e107135
- Li KN, Jain P, He CH, Eun FC, Kang S, Tumber T (2019) Skin vasculature and hair follicle cross-talking associated with stem cell activation and tissue homeostasis. *Elife* 8: e45977
- Liu W, Selever J, Wang D, Lu M-F, Moses KA, Schwartz RJ, Martin JF (2004) Bmp4 signaling is required for outflow-tract septation and branchial-arch artery remodeling. *Proc Natl Acad Sci USA* 101: 4489–4494
- Love MI, Huber W, Anders S (2014) Moderated estimation of fold change and dispersion for RNA-seq data with DESeq2. *Genome Biol* 15: 550
- Luo M, Flood EC, Almeida D, Yan L, Berlin DA, Heerdt PM, Hajjar KA (2017) Annexin A2 supports pulmonary microvascular integrity by linking vascular endothelial cadherin and protein tyrosine phosphatases. *J Exp Med* 214: 2535–2545
- Ma L, Martin JF (2005) Generation of a Bmp2 conditional null allele. *Genesis* 42: 203–206
- Madisen L, Zwingman TA, Sunkin SM, Oh SW, Zariwala HA, Gu H, Ng LL, Palmiter RD, Hawrylycz MJ, Jones AR et al (2010) A robust and high-throughput Cre reporting and characterization system for the whole mouse brain. *Nat Neurosci* 13: 133–140
- Marciel MP, Hoffmann PR (2017) Selenoproteins and Metastasis. *Adv Cancer Res* 136: 85–108
- Martin M (2011) Cutadapt removes adapter sequences from high-throughput sequencing reads. *EMBnet J* 17: 10–12
- Mecklenburg L, Tobin DJ, Müller-Röver S, Handjiski B, Wendt G, Peters EMJ, Pohl S, Moll I, Paus R (2000) Active hair growth (Anagen) is associated with angiogenesis. *J Invest Dermatol* 114: 909–916
- Meszaros M, Yusenko M, Domonkos L, Peterfi L, Kovacs G, Banyai D (2021) Expression of TXNIP is associated with angiogenesis and postoperative relapse of conventional renal cell carcinoma. *Sci Rep* 11: 17200
- Mi H, Muruganujan A, Huang X, Ebert D, Mills C, Guo X, Thomas PD (2019) Protocol update for large-scale genome and gene function analysis with the PANTHER classification system (v.14.0). *Nat Protoc* 14: 703–721
- Mi H, Ebert D, Muruganujan A, Mills C, Albu L-P, Mushayamaha T, Thomas PD (2021) PANTHER version 16: a revised family classification, tree-based classification tool, enhancer regions and extensive API. *Nucleic Acids Res* 49: D394–D403
- Mootha VK, Lindgren CM, Eriksson K-F, Subramanian A, Sihag S, Lehar J, Puigserver P, Carlsson E, Ridderstråle M, Laurila E et al (2003) PGC-1 α -responsive genes involved in oxidative phosphorylation are coordinately downregulated in human diabetes. *Nat Genet* 34: 267–273
- Nikolova-Krstevski V, Yuan L, Le Bras A, Vijayaraj P, Kondo M, Gebauer I, Bhasin M, Carman CV, Oettgen P (2009) ERG is required for the

- differentiation of embryonic stem cells along the endothelial lineage. *BMC Dev Biol* 9: 72
- Norrmén C, Vandeveld W, Ny A, Saharinen P, Gentile M, Haraldsen G, Puolakkainen P, Lukanidin E, Dewerchin M, Alitalo K et al (2010) Liprin (beta)1 is highly expressed in lymphatic vasculature and is important for lymphatic vessel integrity. *Blood* 115: 906–909
- Oh SP, Seki T, Goss KA, Imamura T, Yi Y, Donahoe PK, Li L, Miyazono K, ten Dijke P, Kim S et al (2000) Activin receptor-like kinase 1 modulates transforming growth factor- β 1 signaling in the regulation of angiogenesis. *Proc Natl Acad Sci USA* 97: 2626–2631
- Osorio KM, Lee SE, McDermitt DJ, Waghmare SK, Zhang YV, Woo HN, Tumber T (2008) Runx1 modulates developmental, but not injury-driven, hair follicle stem cell activation. *Development* 135: 1059–1068
- Ostrowska-Podhorodecka Z, Ding I, Norouzi M, McCulloch CA (2022) Impact of Vimentin on regulation of cell signaling and matrix remodeling. *Front Cell Dev Biol* 10: 869069
- Park SO, Lee YJ, Seki T, Hong K-H, Fliess N, Jiang Z, Park A, Wu X, Kaartinen V, Roman BL et al (2008) ALK5- and TGFBR2-independent role of ALK1 in the pathogenesis of hereditary hemorrhagic telangiectasia type 2. *Blood* 111: 633–642
- Park SO, Wankhede M, Lee YJ, Choi E-J, Fliess N, Choe S-W, Oh S-H, Walter G, Raizada MK, Sorg BS et al (2009) Real-time imaging of *de novo* arteriovenous malformation in a mouse model of hereditary hemorrhagic telangiectasia. *J Clin Invest* 119: 3487–3496
- Park H, Furtado J, Poulet M, Chung M, Yun S, Lee S, Sessa WC, Franco CA, Schwartz MA, Eichmann A (2021) Defective flow-migration coupling causes arteriovenous malformations in hereditary hemorrhagic telangiectasia. *Circulation* 144: 805–822
- Peña-Jimenez D, Fontenete S, Megias D, Fustero-Torre C, Graña-Castro O, Castellana D, Loewe R, Perez-Moreno M (2019) Lymphatic vessels interact dynamically with the hair follicle stem cell niche during skin regeneration *in vivo*. *EMBO J* 38: e101688
- Plikus MV, Mayer JA, de la Cruz D, Baker RE, Maini PK, Maxson R, Chuong C-M (2008) Cyclic dermal BMP signalling regulates stem cell activation during hair regeneration. *Nature* 451: 340–344
- Qi JH, Anand-Apte B (2015) Tissue inhibitor of metalloproteinase-3 (TIMP3) promotes endothelial apoptosis via a caspase-independent mechanism. *Apoptosis* 20: 523–534
- Ramasamy SK, Kusumbe AP, Adams RH (2015) Regulation of tissue morphogenesis by endothelial cell-derived signals. *Trends Cell Biol* 25: 148–157
- Rochon ER, Menon PG, Roman BL (2016) Alk1 controls arterial endothelial cell migration in lumenized vessels. *Development* 143: 2593–2602
- Roman BL, Hinck AP (2017) ALK1 signaling in development and disease: new paradigms. *Cell Mol Life Sci* 74: 4539–4560
- Ruiz-Llorente L, Gallardo-Vara E, Rossi E, Smadja DM, Botella LM, Bernabeu C (2017) Endoglin and alk1 as therapeutic targets for hereditary hemorrhagic telangiectasia. *Expert Opin Ther Targets* 21: 933–947
- Scharpfenecker M, van Dinter M, Liu Z, van Bezooijen RL, Zhao Q, Pukac L, Löwik CWGM, ten Dijke P (2007) BMP-9 signals via ALK1 and inhibits bFGF-induced endothelial cell proliferation and VEGF-stimulated angiogenesis. *J Cell Sci* 120: 964–972
- Scheitz CJF, Lee TS, McDermitt DJ, Tumber T (2012) Defining a tissue stem cell-driven Runx1/Stat3 signalling axis in epithelial cancer. *EMBO J* 31: 4124–4139
- Schindelin J, Arganda-Carreras I, Frise E, Kaynig V, Longair M, Pietzsch T, Preibisch S, Rueden C, Saalfeld S, Schmid B et al (2012) Fiji: an open-source platform for biological-image analysis. *Nat Methods* 9: 676–682
- Seki T, Yun J, Oh SP (2003) Arterial endothelium-specific Activin receptor-like kinase 1 expression suggests its role in arterIALIZATION and vascular remodeling. *Circ Res* 93: 682–689
- Shih Y-P, Sun P, Wang A, Lo SH (2015) Tensin1 positively regulates RhoA activity through its interaction with DLC1. *Biochim Biophys Acta* 1853: 3258–3265
- Skobe M, Detmar M (2000) Structure, function, and molecular control of the skin lymphatic system. *J Invest Dermatol Symp Proc* 5: 14–19
- Sörensen I, Adams RH, Gossler A (2009) DLL1-mediated notch activation regulates endothelial identity in mouse fetal arteries. *Blood* 113: 5680–5688
- Srinivasan RS, Dillard ME, Lagutin OV, Lin F-J, Tsai S, Tsai M-J, Samokhvalov IM, Oliver G (2007) Lineage tracing demonstrates the venous origin of the mammalian lymphatic vasculature. *Genes Dev* 21: 2422–2432
- Subramanian A, Tamayo P, Mootha Vamsi K, Mukherjee S, Ebert Benjamin L, Gillette Michael A, Paulovich A, Pomeroy Scott L, Golub Todd R, Lander Eric S et al (2005) Gene set enrichment analysis: a knowledge-based approach for interpreting genome-wide expression profiles. *Proc Natl Acad Sci USA* 102: 15545–15550
- Sun X, Liu S, Wang J, Wei B, Guo C, Chen C, Sun M-Z (2018) Annexin A5 regulates hepatocarcinoma malignancy via CRKI/II-DOCK180-RAC1 integrin and MEK-ERK pathways. *Cell Death Dis* 9: 637
- Tual-Chalot S, Mahmoud M, Allinson KR, Redgrave RE, Zhai Z, Oh SP, Fruttiger M, Arthur HM (2014) Endothelial depletion of Acvrl1 in mice leads to arteriovenous malformations associated with reduced Endoglin expression. *PLoS One* 9: e98646
- Tumber T (2012) Ontogeny and homeostasis of adult epithelial skin stem cells. *Stem Cell Rev* 8: 561–576
- Waghmare SK, Bansal R, Lee J, Zhang YV, McDermitt DJ, Tumber T (2008) Quantitative proliferation dynamics and random chromosome segregation of hair follicle stem cells. *EMBO J* 27: 1309–1320
- Wiater E, Vale W (2003) Inhibin is an antagonist of bone morphogenetic protein signaling *. *J Biol Chem* 278: 7934–7941
- Wu L, Du Y, Lok J, Lo EH, Xing C (2015) Lipocalin-2 enhances angiogenesis in rat brain endothelial cells via reactive oxygen species and iron-dependent mechanisms. *J Neurochem* 132: 622–628
- Yano K, Brown LF, Detmar M (2001) Control of hair growth and follicle size by VEGF-mediated angiogenesis. *J Clin Invest* 107: 409–417
- Yi R (2017) Concise review: mechanisms of quiescent hair follicle stem cell regulation. *Stem Cells* 35: 2323–2330
- Yoon S-Y, Detmar M (2022) Sostdc1 secreted from cutaneous lymphatic vessels acts as a paracrine factor for hair follicle growth. *Curr Issues Mol Biol* 44: 2167–2174
- Zhang YV, Cheong J, Ciapurin N, McDermitt DJ, Tumber T (2009) Distinct self-renewal and differentiation phases in the niche of infrequently dividing hair follicle stem cells. *Cell Stem Cell* 5: 267–278
- Zhang YV, White BS, Shalloway DI, Tumber T (2010) Stem cell dynamics in mouse hair follicles: a story from cell division counting and single cell lineage tracing. *Cell Cycle* 9: 1504–1510
- Zwick RK, Guerrero-Juarez CF, Horsley V, Plikus MV (2018) Anatomical, physiological, and functional diversity of adipose tissue. *Cell Metab* 27: 68–83